

Observations of the Boundary Current System at 26.5°N in the Subtropical North Atlantic Ocean*

ALAN D. CHAVE

Woods Hole Oceanographic Institution, Woods Hole, Massachusetts

DOUGLAS S. LUTHER

Department of Oceanography, University of Hawaii, Honolulu, Hawaii

JEAN H. FILLOUX

Scripps Institution of Oceanography, La Jolla, California

(Manuscript received 11 December 1995, in final form 2 January 1997)

ABSTRACT

Five current meter moorings and four horizontal electric field records spanning June 1990–February 1992 are used to describe the mean structure and variability of the vertically averaged velocity field and volume transport extending 425 km east of Abaco, The Bahamas, at 26.5°N. Examination of zonal and meridional velocity sections shows that, while meandering may explain part of the variability, there is substantial evidence for pulsation of the core DWBC velocity in the record. Intermittently strong northward flow is observed 225 km east of Abaco that is significantly coherent and out of phase with the currents closer to the boundary at periods of 50–100 d and longer, suggesting recirculation. This is never observed 315 km offshore. At 380 km offshore and extending east at least 60 km, a strong, dominantly southward flow is observed that is coherent with both that near Abaco (in phase) and in the intervening recirculation zone (out of phase) at long periods. The net mean transport (over 17 months) from Abaco to 325 km offshore, spanning the recirculation region, is -17 Sv ($\text{Sv} \equiv 10^6 \text{ m}^3 \text{ s}^{-1}$). The transport exhibits robust annual variability, and correction for the bias from the annual cycle in the 17-month dataset reduces the net mean transport at 325 km to -13.6 Sv. Allowing for a northward Antilles Current transport of 5.1 Sv yields a mean southward DWBC transport corrected for local recirculation of about 18.5 Sv, in approximate agreement with the thermohaline input from the northern North Atlantic. Comparison of transport time series from the Florida Current with that extending 125 km east of Abaco demonstrates significant and out of phase coherence over the period range 100–250 d. The coherence decreases as the Abaco transport is integrated farther to the east.

1. Introduction

The formation of North Atlantic Deep Water by high latitude convective processes leads to a thermohaline circulation, which is manifest as a deep western boundary current (DWBC). For the purposes of this paper, DWBC means a boundary flow with a distinct velocity profile flowing generally southward along the east coast of North America, typically but not always at depths of 1000–4000 m and within 150 km of the continental shelf break, but which may meander and/or break into discrete

filaments along its path. The DWBC transport must be balanced on average by a warm return flow in the thermocline, completing the meridional overturning. While deep-water production is episodic and displays substantial interannual variability, Schmitz and McCartney (1993) estimate a total DWBC transport in the mean of 16 Sv ($1 \text{ Sv} \equiv 10^6 \text{ m}^3 \text{ s}^{-1}$). Schmitz (1995) has documented the general support for 12–15 Sv of overall deep-water formation and its transport to the South Atlantic and beyond. Thus, a total thermohaline transport of as much as 16 Sv is expected to pass south through the North Atlantic. Direct measurements of DWBC transport south of the subpolar gyre consistently give transports that are larger than this value (Hogg and Johns 1995), suggesting that a substantial component is recirculating into the ocean's interior. As used in this paper, recirculation is a permanent flow with the opposite sense to the DWBC, typically but not necessarily to its east, which is fed by and feeds water to the DWBC,

*Woods Hole Oceanographic Institution Contribution Number 9453.

Corresponding author address: Dr. Alan D. Chave, Department of Geology & Geophysics, Woods Hole Oceanographic Institution, Woods Hole, MA 02543.
E-mail: alan@faraday.whoi.edu

and which may have dimensions ranging from meso- to gyre scale. Pervasive deep recirculation is supported by tracer measurements, which indicate enhanced ventilation of the deep Western North Atlantic (e.g., Fine 1995).

In the North Atlantic near 26°N, both the deep southward flow and the thermocline return are concentrated near the western boundary: the poleward Florida Current (FC), which is confined to the Florida Straits, and the DWBC transiting on the east side of the Bahamas Platform. The FC is very well characterized, displaying a mean transport of about 32 Sv at 27°N with an annual cycle amplitude of 2.2 Sv (Larsen 1992). Schmitz and Richardson (1991) have shown that 13 Sv of this transport is due to a warm thermohaline return flow from the South Atlantic, with the remainder resulting from a Sverdrup balance with the winds east of 55°–60°W (Schmitz et al. 1992). In addition, the poleward Antilles Current (AC) flows east of the Bahamas Platform, although its role in the thermohaline flow is unclear, and it may, in fact, be purely wind driven. Neither the AC nor the DWBC are as well understood as the FC, reflecting the complexity and temporal variability of the flow regime east of Abaco. Boundary current moorings have been maintained along 26.5°N for about six years, and the data display transport variations of over 100 Sv on 100-d timescales or less and a substantial annual cycle (Lee et al. 1990, 1996; hereafter LJSZ90 and LJZF96). A weak AC exists in the thermocline close to the Bahamas Platform, carrying a few Sverdrups to the north. LJZF96 attribute the DWBC variability to meandering, and after attempting to correct for intervals when the DWBC moves east of the boundary mooring array, they suggest an apparent mean southward transport of about 40 Sv. In this paper, meandering is a situation where the DWBC core moves offshore from its usual position, with the concomitant implication that there is minimal fluctuation of the mean transport.

In the present work, the boundary mooring data from the Western Atlantic Thermohaline Transport Study (WATTS) interval (June 1990–February 1992) are re-examined with the addition of four records of the horizontal electric field (HEF), which give the vertically integrated water velocity. These data fill and extend the mooring array to 425 km east of Abaco. Section 2 describes the data and estimation of the vertically averaged velocity (VAV) from them. Section 3 reports on the zonal and meridional velocity sections and shows that, while meandering may explain some of the variability, there is substantial evidence for pulsation of the core velocity and transport of the DWBC. Strong but fluctuating northward recirculation is observed 225 km offshore of Abaco that is significantly coherent and out of phase with that closer to the boundary at periods longer than 50–100 d. The recirculation is never observed at a mooring 315 km offshore. Eastward of 73°W (about 380 km offshore), strong and dominantly southward flow is seen, which is coherent with both that near the

boundary (in phase) and the intervening recirculation region (out of phase) at long periods. Section 4 describes the spectral character of the data, further elucidating the main observations in section 3. Section 5 describes estimation of meridional transport from the data. The net mean transport after integration from the boundary to the end of the recirculation region at 325 km is -17 Sv. Correction for the strong observed annual cycle in the 17-month series reduces the net mean transport to -13.6 Sv. Section 6 reveals the existence of a significant out of phase relationship between FC and Abaco transport out to 125 km over the period range of 100–250 d. Section 7 contains a discussion of some of the principal findings.

2. Observations

a. Geographic setting and data

Study of DWBC structure and variability at 26.5°N off Abaco, The Bahamas, began under the NOAA STACS program in mid 1985. LJZF96 describe four deployments of current meter moorings, of which WATTS was the last and is utilized in the present work. The WATTS deployment consisted of four moorings located 15, 55, 89, and 131 km from the boundary (taken here to be at 77°00'W) from June 1990 to February 1992, which were intended as a transport-resolving array (Fig. 1). Mooring A was placed near the top of the Bahamas Escarpment at 900-m depth within the strong northward thermocline flow detected in earlier experiments (LJSZ90). Moorings B and C were located near the mean core of the DWBC in deep water (about 4800 m). Mooring D was placed near the presumed eastern edge of the DWBC. A fifth mooring E was located 316 km from the boundary on the eastern side of a small topographic rise that is a southward extension of the Blake–Bahamas Outer Ridge, which is expected to control the deep recirculation (Leaman and Harris 1990; LJSZ90).

From September 1990 to February 1992, the WATTS moorings were augmented with a set of 11 horizontal electrometers placed at 30–50 km spacing along 26.5°N. As discussed in Chave and Luther (1990) and appendix A, measurement of the HEF yields an accurate estimate of the vertically integrated water velocity. Due to faulty lithium batteries, data return from the electrometers was poor, and only four complete records were obtained. Fortunately, these occur at key locations that substantially enhance the information from the moorings (Fig. 1). Site E2 was located at 4550-m depth immediately at the base of the Bahamas Escarpment and landward of mooring B. Site E7 is near the crest of the topographic rise between moorings D and E. Sites E10 and E11 are east of mooring E and extend the array out to 437 km from Abaco.

The mooring data are described in Zantopp et al. (1994). Instruments were placed at nominal depths of

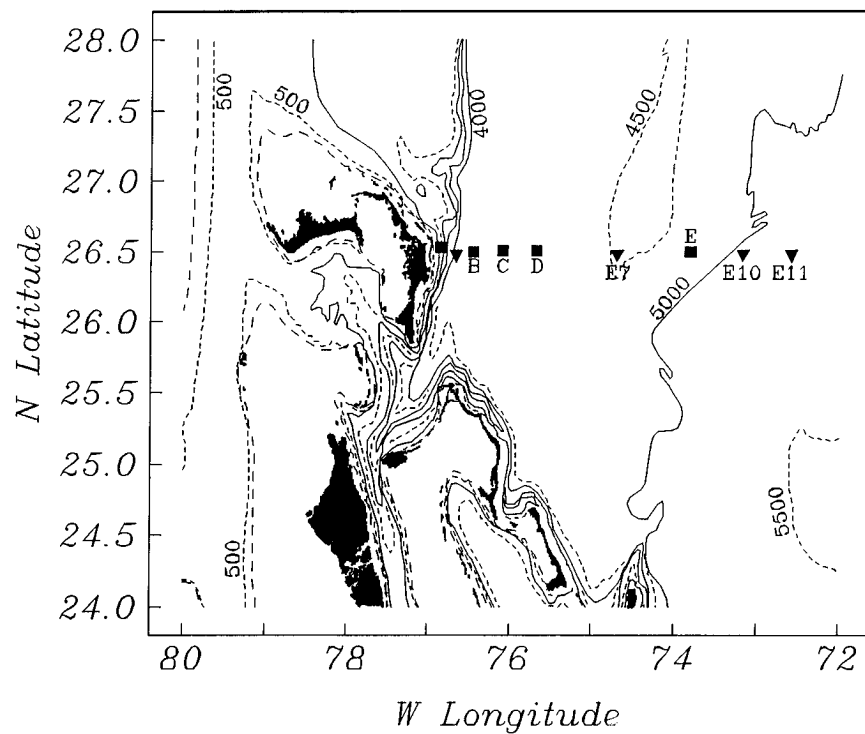


FIG. 1. Bathymetric map showing the major islands in heavy black together with major depth contours beginning with 200 m (long dashed line), then every 500 m starting at 500 m (alternating between short dashed and solid lines). The solid squares show the locations of the five moorings, while the solid triangles show the locations of the four HEF recorders. These are marked except for the sites A and E2 at the western end of the line.

100, 400, 800, 1200, 2000, 3000, and 4000 m on moorings B–E. Mooring A used only the first three depths due to the shallowness of the site. A mixture of Aanderaa, VACM, and VMCM instruments were utilized, with the former two types containing pressure and temperature sensors. In addition, moorings D and E con-

tained additional temperature–pressure recorders at nominal depths of 200 and 1400 m. Table 1 summarizes the available data. The VMCM records from the 2000-m level on mooring D and the 1200-m level on mooring E were discarded due to pervasive rotor stalling. The temperature record from the 200-m level on mooring D was not used because of anomalously low amplitude, which cannot be explained by a permanent weak gradient of the mean temperature profile at that depth. Because of other instrument failures, there are no current data from site D at 2000 and 3000 m and from site E at 1200 and 2000 m for the second half of the experiment. After data editing, all of the time series were decimated to 12-h samples after low passing with a 40-hour Lanczos filter. The pressure records show that substantial (as much as 250 m) and sharply episodic depth excursions were experienced, especially at moorings B–D.

The HEF was measured using technology described by Filloux (1987). The potential difference over a 3-m span salt bridge was determined using a high impedance recording voltmeter and silver–silver chloride electrodes at 16 samples/hour. An electrode reversing technique was employed to remove electrode drift, yielding a measurement that is accurate to DC. After data editing, the HEF time series were low-pass filtered using a Slepian or discrete prolate spheroidal sequence (Percival and

TABLE 1. Instrument positions, depths, and data type.

Site	Lat (°N)	Long (°W)	Depth (m)	Data type
A	26.528	76.848	900	100(V, T) 400(V, T, P) 800(V, T, P)
E2	26.479	76.662	4550	HEF
B	26.497	76.450	4838	180(V, T) 480(V, T, P) 880(V, T, P) 1280(V, T, P) 2080(V, T) 3080(V, T) 4080(V, T)
C	26.500	76.100	4808	180(V, T, P) 480(V, T, P) 880(V, T, P) 1280(V, T, P) 2080(V, T) 3080(V, T) 4080(V, T)
D	26.500	75.683	4685	180(V, T) 480(V, T, P) 880(V, T, P) 1280(V, T) 1480(T, P) 2080(T) 3080(V, T) 4080(V, T)
E7	26.483	74.703	4330	HEF
E	26.492	73.820	4800	180(V, T) 280(T, P) 440(V, T, P) 1200(T) 1400(T, P) 2000(V, T) 3000(V, T) 4000(V)
E10	26.480	73.191	4901	HEF
E11	26.478	72.602	4958	HEF

Walden 1993) that attenuates the semidiurnal tide by 60 dB, and subsampled at 12-h intervals.

b. Computation of the vertically averaged water velocity

Estimates of the VAV from the moorings and HEF recorders form the basis for most of the analyses in this paper. To estimate the VAV from moored current meters, it is convenient to expand the velocity time series in terms of dynamical normal modes. Despite that the dynamical normal modes are obtained from the equations of motion under certain simplifying assumptions, such as no mean flow and linearity, this does not mean that those conditions are being assumed for the ocean's dynamics. Rather, the normal modes are a convenient basis set that mimics the ocean's behavior and hence has desirable convergence properties and is also easily integrated over the water column.

The computational procedure is as follows: a set of dynamical normal modes based on the zonal-average buoyancy frequency profile for 27.5°N in Levitus (1982) and the water depth at each mooring are computed numerically using a variational approach. A simple correction for mooring motion was derived by assuming that each mooring responds tautly to the current. This allows the true depth of each current meter to be computed from the available pressure records as a function of time. Tests of the accuracy of the taut mooring assumption were performed by leaving out individual pressure records and comparing the computed and measured depths; the agreement was typically better than 10 m except for intervals of rapid change at mooring B. Given the observed velocity time series and computed instrument depths, the amplitudes of the velocity normal modes can be computed as a function of time using a least squares approach, and the modal fit is then removed from each current meter record to yield a residual time series, which is typically small compared to the original record. Numerical integration of the normal mode expansion, parameterized in terms of cubic splines, together with trapezoidal rule integration of the residual, yields time series of the VAV.

As a test of the accuracy of the vertical averaging method, the first 286 d of meridional velocity data at mooring B, when seven current meters were operational, were also integrated using the trapezoidal rule and assuming that the velocity observed at the top and bottom current meters continues unchanged to the sea surface and seafloor, respectively. The mean (rms) differences between the modal expansion and trapezoidal integrations are 0.05 (0.23) cm s⁻¹, which are both substantially smaller than the typical accuracy of a current meter. Thus, the result does not depend strongly on the integration algorithm. As a test of the sensitivity to reduced sampling, the VAV was computed using a 3-mode expansion for the same 286-d interval after leaving out a single current meter and compared to the result for all

seven current meters. Deleting the records at 180, 1280, and 3080 m changed the mean (rms) differences by -0.18 (0.65), -0.22 (0.44), and -0.21 (1.18) cm s⁻¹, respectively. Deleting both the 180- and 1280-m records, as happens for the second half of the record due to instrument failures, changes the mean (rms) differences by -0.30 (0.77) cm s⁻¹. Thus, the modal expansion method is robust to a reasonable level of missing data. While it is difficult to quantify the accuracy of the mooring-derived VAV estimate, a conservative value is of order 1 cm s⁻¹ based on tests like those described above.

Some physical variables are natural spatial integrals of oceanic water motion and hence permit the isolation of physical processes that might otherwise be difficult to examine because of the superposition of many phenomena at a single measurement point. The HEF is one such variable, being proportional to the seawater conductivity-weighted, vertically integrated water velocity averaged around the measurement site. Both Sanford (1971) and Chave and Luther (1990) have derived a theoretical relationship between the HEF and the water velocity field formally valid for a flat-bottomed ocean. A brief recapitulation of the theory and a demonstration that the HEF directly measures the VAV at least as accurately as the moored current meters may be found in appendix A. The comparisons in appendix A show that the HEF directly yields the VAV with a total error of about 1 cm s⁻¹ throughout the Abaco region. In addition, appendix A also shows that the VAV is nearly equivalent to the vertically averaged deep flow (from 800 m to the seafloor) in the boundary region and hence serves as a suitable proxy for DWBC variability.

3. The Abaco velocity section

Figures 2 and 3 show, respectively, the raw 2-d low-passed, 12-h sampled, zonal and meridional VAV time series for all sites. In these and succeeding data plots, time is referenced to 0000 UTC 1 June 1990. The most prominent visual feature in the zonal velocity data is a subtle, very low frequency, quasiperiodic variation that is in phase across the array. This is manifest by an eastward maximum around day 200 and a second eastward maximum near day 550, both of which are in winter. The eastward peak is especially evident at moorings C and D, from which point it can be traced to the east as far as E10, although with weakening amplitude, and to the west as far as E2. There is also a westward maximum near day 150 and again around day 430, both of which are in fall. These are again most clearly visible at moorings C and D, but the first westward peak cannot be seen farther to the east and is evident only in the boundary current region. The second of the two westward maxima in zonal velocity is much sharper and deeper, especially at sites C and D, but again is difficult to trace outside the boundary current.

The meridional velocity has a more energetic char-

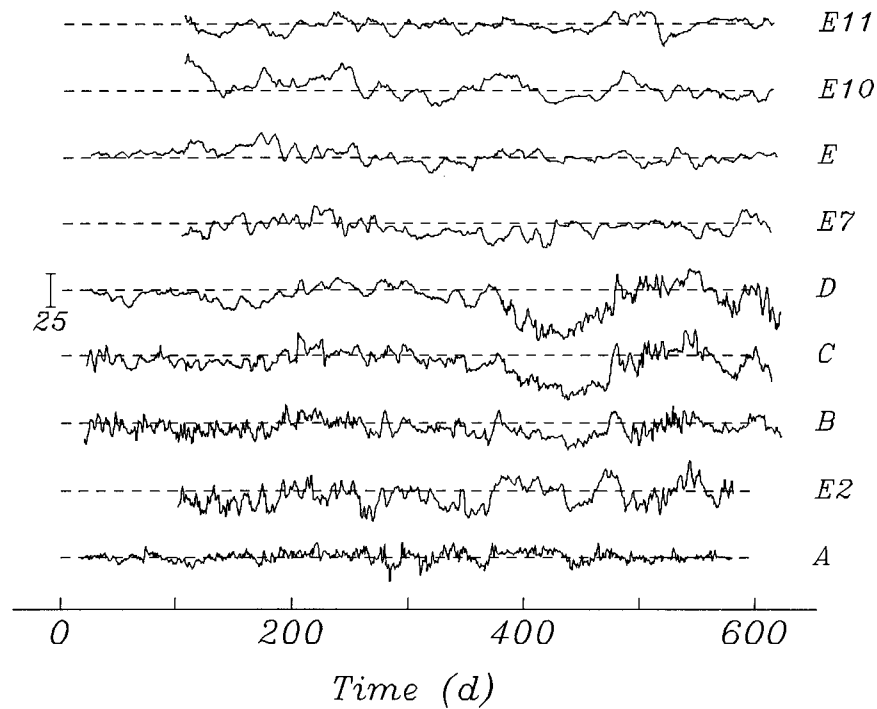


FIG. 2. The zonal time series of VAV for the mooring and HEF sites. The time reference is 0000 UTC 1 June 1990, and the scale in cm s^{-1} is shown at the left. All data have been low-passed filtered with a 2-d cutoff to remove tidal variations and sampled at 12-h intervals.

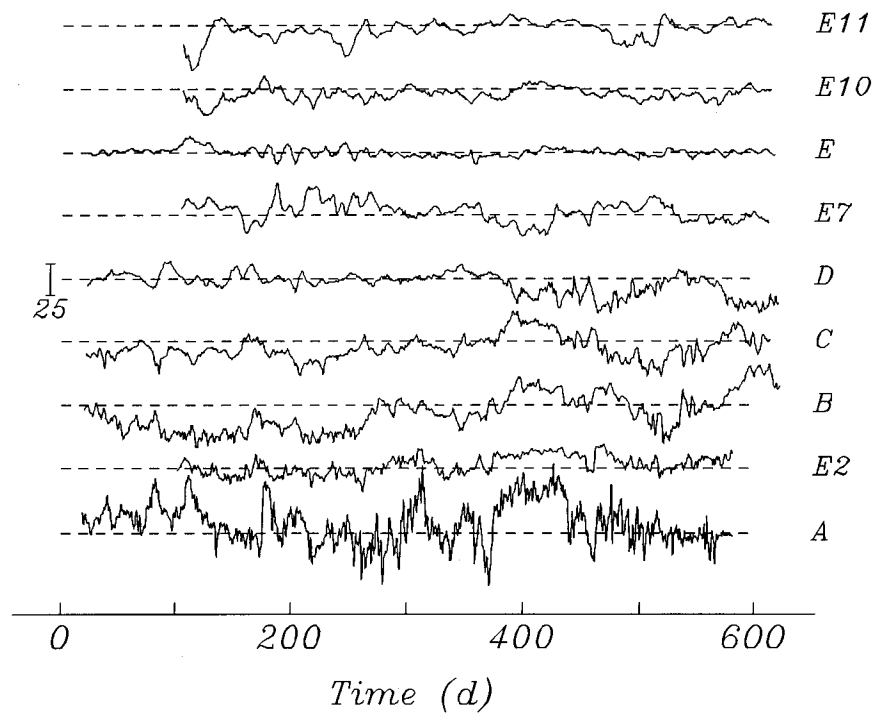


FIG. 3. The meridional time series of VAV for the mooring and HEF sites. The time reference is 0000 UTC 1 June 1990, and the scale in cm s^{-1} is shown at the left. All data have been low-passed filtered with a 2-d cutoff to remove tidal variations and sampled at 12-h intervals.

acter than the zonal component, especially near Abaco. However, it should be remembered that mooring A is in water only 900 m deep, and hence the fluctuations in the transport per unit width (VAV times water depth) at that location are reduced by a factor of about 5 relative to that at the remaining sites. There are several major features in the meridional velocity to which attention will be drawn. First, there are intervals of strong southward flow near the boundary (sites B–D) interspersed with northward flow. LJSZ90 and LJZF96 have shown that the mean DWBC core, which dominates the VAV when present, is centered between 2000- and 3000-m depth and approximately 50 km offshore, or near mooring B, and have interpreted its variability as onshore–offshore meandering of the core. Especially, LJZF96 identify the northward flow at moorings B and C around day 400 in Fig. 3, with concomitant southward flow at mooring D, as an indication of a significant offshore meander of the DWBC together with generation of an anticyclonic eddy inshore. However, the meridional currents at moorings B, C, and D, along with electrometer E7, shown in Fig. 3 suggest a more complicated temporal evolution of the currents. A long period of strong southward flow centered at mooring B, but also evident at E2 and C, comes to an end at about day 270 (approximately 1 March 1991). For at least the next 45 days there are only very weak meridional VAVs at B, C, D, and E7, followed by another 60 days of weak southward VAV at B. Such weak VAVs could be explained by large upper-ocean currents in opposition to the flow of the DWBC, but this is not observed at the moorings. It might be argued that southward flow went undetected during this time period between D and E7 (a distance of a little under 100 km), but if the DWBC were there, it did not meander to that location since mooring D shows only weak southward VAV for the first 350 days of the record. Consequently, the strong DWBC indicated by strong VAVs prior to day 270 has not meandered offshore, but has simply vanished. Note that there are also weak zonal VAVs (Fig. 2) during the same time period.

Beginning around day 365, southward VAV shows up 226 km offshore at E7 and soon thereafter at D. Concurrently, northward flow appears at A, E2, B, and C. Despite the involvement of the upper-ocean currents, as indicated by northward flow at A, the deep flow is strongly northward according to the moorings. The association of this variability with exceptional westward VAVs (Fig. 2) indicates the presence of a large eddy motion. A possible explanation for the sequence of events from day 270 to 470 is that a meander formed in the DWBC to the north of the array, temporarily weakening the downstream flow, and then the eddy passed into the array. Whatever the explanation, the sequence of variability seen in Figs. 2 and 3 from day 270 to 470 is not well explained as offshore–onshore meandering.

Second, there is no interval during which the strong-

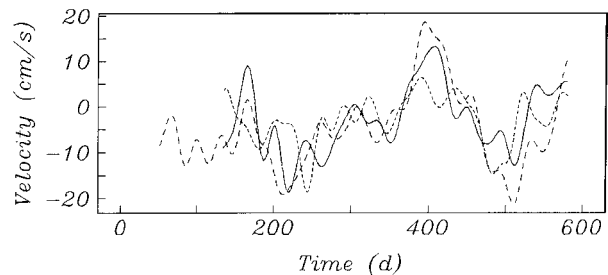


FIG. 4. The meridional velocity time series for C (long dashed line), E7 (reversed in sign; solid line), and E11 (short dashed line) after low-pass filtering the data with a Slepian sequence having a 30-d cutoff. The time reference is 0000 UTC 1 June 1990.

est part of the DWBC core directly abuts the Bahamas Escarpment, and it appears to consistently remain at least 30–50 km offshore. The strong southward excursions in the VAV seen at mooring B are not ever observed at E2 at the base of the Bahamas Escarpment. Mooring A is dominated by a strong, generally northward thermocline AC (LJZF96), which was inferred to extend offshore as far as E2 with reduced amplitude. It appears that the E2 data reflect a combination of the shallow AC and a much attenuated DWBC flow, but a single measurement of the VAV is not adequate to determine the relative weighting.

Third, there is evidence for recirculation at site E7 located 228 km offshore, while mooring E at 316 km appears to be close to a null in meridional velocity. During the strong, steady southward flow at mooring B from the beginning of the record to day 260, E7 displays a fluctuating but generally northward velocity that is again seen around day 500 at the next strong southward event near Abaco. There is no visual evidence for a recirculating component at mooring E. Figure 4 shows 30-day low-passed versions of the meridional velocity at C, E7 (reversed in sign), and E11. This further reinforces the recirculation interpretation for the low-frequency variability at E7 and also suggests significant coherence of the flow at E11 both with that in the recirculation region and that near the boundary. The form of the correlation is more suggestive of a standing pattern than of propagating features. Furthermore, the visual coherence occurs over a variety of timescales, and is not confined to anything like an annual component.

The above assertions are reinforced by examining a stick plot of the VAV time series (Fig. 5) after low-pass filtering them with a Slepian sequence having a 15-d cutoff to remove the highest frequency fluctuations. In particular, this display strongly suggests that the DWBC variability is not due to simple zonal meandering of a dominantly meridional current, but rather involves significant shifts in azimuth in addition to zonal motion. This is especially obvious from days 300 to the end of the record, where the landward-moving southward core of Fig. 3 is actually seen to start out with more of a westward than a southward velocity. Similar shifts in

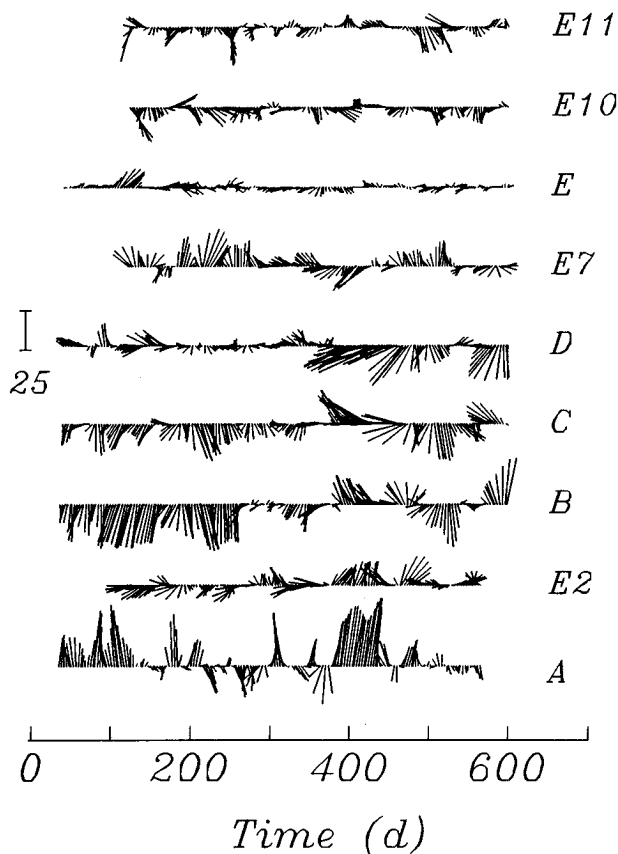


FIG. 5. Stick plot of the vertically averaged velocity time series at all sites after low-pass filtering with a Slepian sequence having a 15-d cutoff and 60 dB of stopband attenuation. The velocity is plotted at 3-d intervals, and the reference time is 0000 UTC 1 June 1990. The velocity scale (in cm s^{-1}) is shown at the left.

the current azimuth are seen in the LADCP sections collected in the two years subsequent to WATTS and presented by Hacker et al. (1996).

Hydrographic data collected in June–July 1990 present a snapshot view of the circulation east of the Bahamas consistent with the above (see Johns et al. 1997, Figs. 8a and 10). In particular, they show a recirculation gyre centered at about 75°W , with northward flow between 180 and 270 km offshore, and strong southward flow to the east extending out at least 500 km from Abaco. Their synoptic picture suggests that the DWBC separates into two components as it rounds the Blake–Bahama Outer Ridge near 29°N , 72°W with one part continuing along the Blake Escarpment and remaining separated by a recirculation gyre from the remaining offshore portion. The bathymetry suggests that the branches probably rejoin south of 23°N , although data to show this are lacking. Mean horizontal water velocities computed from RAFOS float trajectories (see Leaman and Vertes 1996, Fig. 10) further support the observed recirculation pattern along 26°N . Four of five absolute velocity sections collected with shipboard LADCP in the two years subsequent to WATTS (Hacker

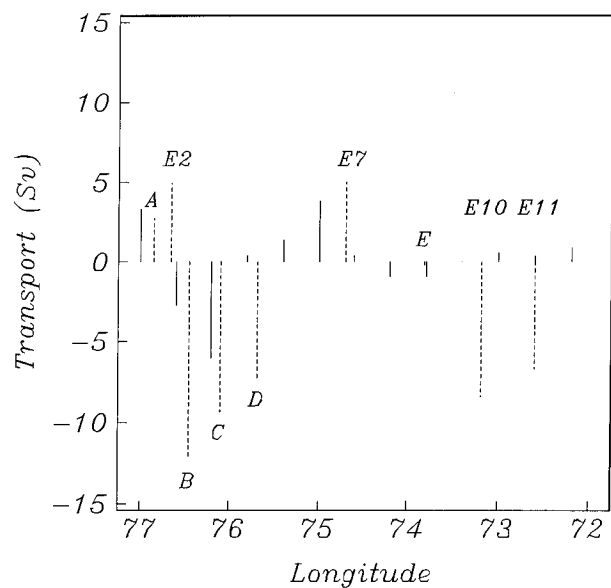


FIG. 6. The solid lines show the zonal distribution of mean meridional volume transport computed for $2/5$ degree longitude bins off Abaco from an average of the last 5 years of a 25-yr CME model run. The dashed lines are the observed mean meridional transport at the nine Abaco line sites computed by assuming each site is $2/5$ degree wide.

et al. 1996) show northward flow near the topographic high at 74.5°W , although the maximum northward flow is not necessarily found at the longitude of E7 near the top of the topographic rise. The LADCP sections also show generally southward velocity east of 73°W (356 km offshore) although there is considerable variability over time. Despite very different temporal and spatial averaging properties, all of these results support the existence of recirculation over some part of the region 150–300 km east of Abaco and provide qualitative support for the suggestion of Leaman and Harris (1990) and LJSZ90 that the topographic rise centered at 74.5°W controls some part of the DWBC recirculation. In addition, they suggest that the flow displays generally southward velocity with large variability to the east of 73°W extending to at least 400–500 km east of Abaco.

LJZF96 (their Fig. 11) presented the zonal distribution of mean volume transport above and below 800-m depth computed from the last five years of a 25-year CME model run (Bryan and Holland 1989). Figure 6 shows these results replotted for the entire water column together with the mean meridional velocity from the nine observation sites converted to transport over the same $2/5$ degree bins used in the model. As noted by LJZF96, the CME underpredicts the southward DWBC transport and yields a much larger net northward transport than is observed in the upper layer out to 300 km from Abaco. It also underestimates the width of the DWBC, as seen by the large discrepancy at site D, and generally displays more variability than the ocean in this region. However, it yields a reasonable value for

the zonal scale of the recirculation, as demonstrated by the approximate agreement of the model with the observed mean transports at E7 and E. This recirculation is quite tight, having a width of less than 200 km. The model fails to predict the observed strong southward transport at E10 and E11.

4. Spectral character of the variability

Auto- and cross-spectra of the VAV further elucidate some of the points made in the last section. In this paper, all spectra will be computed using the multiple window expansion of Thomson (1982), which offers the best possible bias protection for a given choice of spectral bandwidth. Unlike traditional band-averaged estimates, the bandwidth of multiple window estimates remains constant across frequency, and the computed spectrum may be thought of as the true spectrum convolved with a boxcar filter of constant bandwidth. The Abaco spectra divide into four regimes. The first of these consists of site A in the AC, where the zonal velocity spectrum is more than an order of magnitude weaker than the meridional one and most of the variance is concentrated in the 30–200 d band. E2 is transitional toward the second type of spectra, which are observed in the boundary current at sites B–D. Figure 7 (top) shows variance conserving spectra for site C. In this region, most of the variance is concentrated at periods longer than 100 d, with substantially weaker peaks at about 30 and 14 d. The zonal and meridional variances are comparable, except at site B where the meridional variance is about five times larger at long periods. The third spectral regime consists of E7 and E. While there is site-to-site variability, there is typically substantially more variance at short relative to long periods than in the boundary current. Figure 7 (bottom) shows spectra for E7, which display comparable zonal and meridional energy that is concentrated around 140, 30, and 16 d. The mooring E results are comparable except that the 16 day peak dominates the meridional spectrum. The last class of spectra are at the two easternmost sites, where the variance is broadly concentrated in the 25–200 day band and of comparable magnitude in the zonal and meridional components.

For the zonal velocity at sites B–D, two-point coherences show that all adjacent elements are significantly coherent (using a 95% criterion) and appropriately in phase at periods longer than 20 d. In addition, all nonadjacent elements between B and E7 are typically coherent and in phase at periods longer than 50 d. This behavior is visually evident in Fig. 2. At the ends of the line, the coherence is typically weak. Site E2 is strongly coherent and in phase with B only in the 25–100 d band and almost incoherent with A, and both A and E2 exhibit only scattered coherent bands with more distant sites. Eastward of E7, there are only isolated coherent bands between adjacent elements, and no longer range coherence.

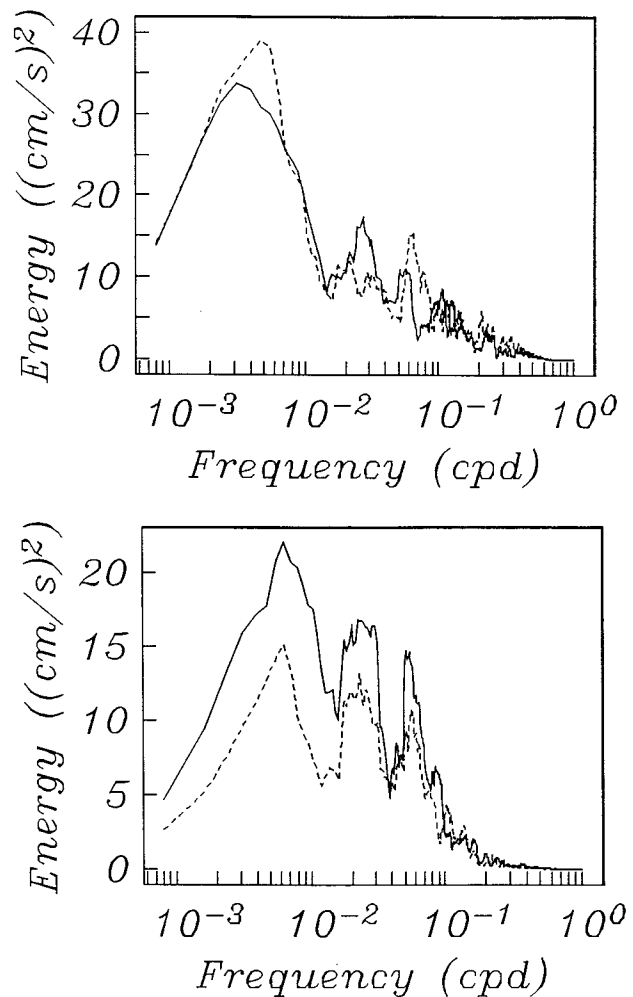


FIG. 7. Multiple prolate window power spectra in variance conserving form for the meridional (solid) and zonal (dashed) vertically averaged velocities at site C (top panel) and site E7 (bottom panel). The estimates have a bandwidth of 0.01 cpd and each frequency has about 14 degrees of freedom. Note that the scales are different for the two sites.

The meridional velocity two-point coherences display four key features at long periods. First, adjacent elements are typically not significantly coherent except for sites A through C near Abaco and E10–E11. The four westernmost elements are approximately in phase at periods longer than 50–100 d. Second, sites B, C, E10, and E11 all are significantly coherent and in phase, but are all nearly out of phase with E7 at periods longer than 50–100 d (Fig. 8). All of the Abaco line sites are out of phase with E7 as the frequency approaches the DC limit with the exception of mooring D, which is in phase. It is more difficult to reach meaningful conclusions about the circulation at site E due to very weak long period coherence. These observations strongly support the visual evidence in Figs. 3–6 that some recirculation occurs near the middle of the Abaco line and further intimate that the topographic rise on which E7

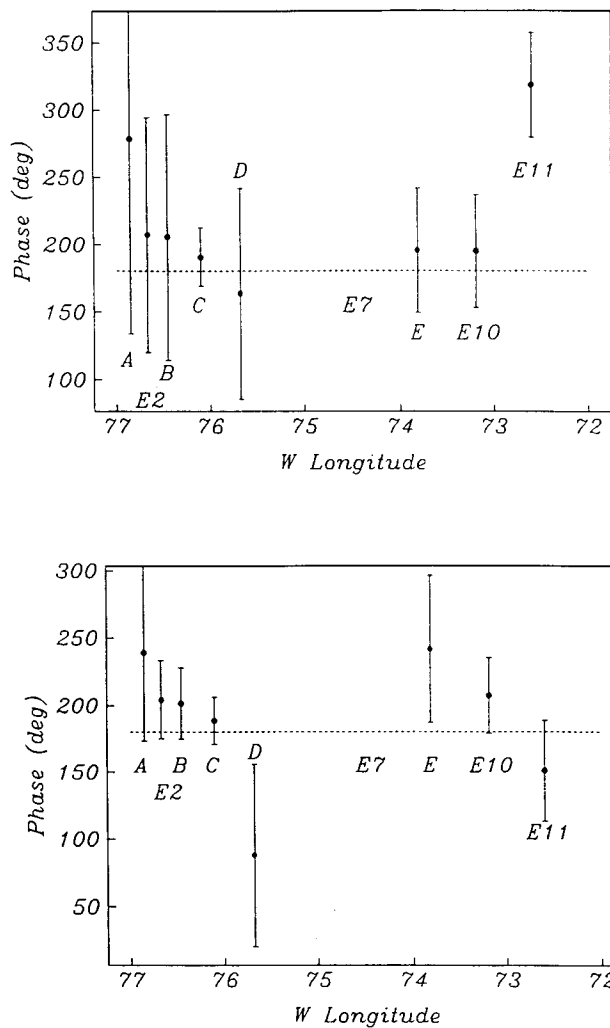


FIG. 8. The phase of the two-point coherence of the meridional vertically averaged velocity between the site listed at the bottom of the plot and site E7 at a period of 62.5 d (bottom) and 125 d (top). The horizontal dashed line indicates 180°. The error bars are the approximate double-sided 95% confidence limits (twice the standard error) computed using the nonparametric jackknife (Thomson and Chave 1991). A positive phase means that site E7 leads the listed site.

lies may play a role in steering that recirculation. The data are suggestive of a standing pattern whereby stronger nearshore southward transport is accompanied by coincident stronger northward flow around E7 and stronger southward flow at E10 and E11. They also imply that the location of mooring D may play a role in the recirculation at some times. The weak coherence with mooring E suggests that very little of the recirculating flow occurs to the east of the rise, as is also supported by the approximate velocity null at that location (Figs. 3–6). Third, the easternmost boundary current mooring D shows curiously weak long period coherence with the rest of the line. Only sites E2 and B are significantly coherent with D, and both are nearly out of phase with

it. This may reflect meandering, which places the DWBC at site D at some times and the western edge of the recirculation at that location at other times. Finally, the two eastern sites, E10 and E11, are significantly coherent at the longest periods (>100 d) with boundary current elements B and C with a nearly in phase response and with site E7 with an approximately out of phase response. These observations suggest that the boundary current system at this location is displaying complex long-range interactions that extend offshore to at least 425 km.

LJZF96 showed that propagating components can be identified in the upper 800 m of the water column at sites A–D at 100-d period, but not below that depth. They identified a westward propagating baroclinic component with an apparent wavelength of 335 km. Attempts to find a propagating component in the VAV did not work as satisfactorily as the standing pattern interpretation described above. For example, the hypothesis that a linear relationship exists between station separation and phase at 125 d can be rejected at the 95% confidence level. Nevertheless, there may be weak propagating components present in the VAV, especially near Abaco, which contribute to the observed variance at long periods. There is also coherence between sites at periods shorter than 50–100 d, often with a nonzero phase suggestive of propagation. However, this is not sufficiently consistent to be definitive, probably indicating baroclinicity and concomitant weakness in the VAV, and hence will not be emphasized. It should be noted that LJZF96 report westward propagating components in the meridional velocity at periods of 30 d that are confined to the top 800 m of the water column, but nothing below the upper ocean.

Some of these relationships may be further elucidated using a frequency domain eigenvector (sometimes called empirical orthogonal function) analysis. A multiple window version of this technique is described in appendix B. Figure 9 shows the squared singular values for the first three eigenvectors after normalization such that the sum of the squared singular values at a given frequency is unity, so that the plotted quantity represents the fractional total power in all of the data series accounted for by each eigenvector. While there is variability across frequency, the first through third eigenvectors account for about 35–45%, 20–25%, and 10–15% of the total data variance, respectively.

Figure 10 shows the first principal component (PC, sometimes called empirical orthogonal function amplitude) at the top and the squared coherence of the first PC with the data at the bottom for the periods specified on the right. The behavior of the PCs divides at roughly 30 d. For periods of 30 d and longer, the coherence of the data with the PC is typically significant at the 95% level for the zonal velocity at sites C, D, and E10, and the meridional velocity at site E11, with the zonal velocities being approximately in phase across the Abaco line and the meridional velocity having a phase of about

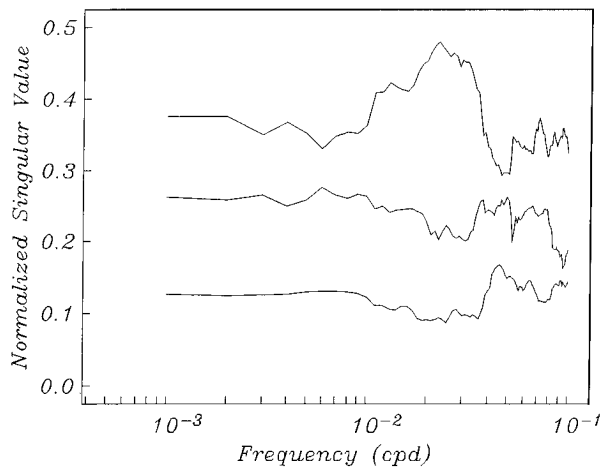


FIG. 9. The first three squared singular values from a frequency-domain principal components analysis of the zonal and meridional vertically averaged velocity for all sites along the Abaco line. The singular values have been normalized so that the sum of their squares is unity, and hence the plotted quantities represent the fractional power in all of the data series accounted for by each principal component at a given frequency.

180° relative to the zonal terms. As period decreases toward 30 d, the PC becomes increasingly confined to the westward sites. At periods shorter than 30 d, the coherence is significant for the meridional velocity at sites B–D and (for some periods) E7. The behavior is nearly independent of period from 10 to 30 d, and the PC is clearly due to meandering of the boundary current with an increasing phase from west to east. The PC is largest for site D, suggesting that it is dominated by intervals when the DWBC is offshore. Note also that C and E7 are approximately in phase so that this PC is not indicative of recirculation.

Figure 11 shows the second PC and its squared coherence with the data. As for the first PC, there is a rough division in behavior at 30 d. At longer periods, the pattern is reminiscent of larger-scale meandering ranging from sites A to D. At periods from 10 to 30 d, the PC is largely confined to the eastern end of the line and is not readily interpretable.

Figure 12 shows the third PC and its squared coherence with the data. At periods longer than 25–30 d, the third PC is a recirculation mode involving sites B–C (meridional) with site E7 (meridional), with the latter typically out of phase with sites B and C. At shorter periods, the PC is not physically interpretable.

5. Meridional transport for the Abaco section

Meridional total water column volume transport was computed over various ranges out from Abaco using the time series of meridional VAV from the moorings and HEF recorders. At a given time, the meridional VAV scaled by the water depth at each site yields the transport per unit width, which can be integrated zonally eastward

from Abaco (where the transport is zero) to yield the section transport. A comparison was made between trapezoidal rule, cubic spline, and piecewise overlapping parabola (Jones 1969) integration to get transport. Cubic splines, including those under tension, persistently insert extraneous inflection points into the curve of transport per unit width, resulting in unsatisfactory artifacts in the estimate. Trapezoidal rule and piecewise parabola integration give nearly identical mean values, but the parabola method consistently exhibits larger peak values and significant differences from the trapezoidal rule result when the transport is changing rapidly. Because it is more conservative, trapezoidal rule integration was used to get final transports. Leaving out the HEF data and using only moorings A–D yields mean transports and standard deviations at 85 and 125 km of -13.3 ± 29.9 and -21.7 ± 34.8 Sv, respectively. This compares to -17.6 ± 30.4 and -25.9 ± 33.8 Sv over the same distances from LJZF96 using an alternate methodology, a difference of 4.2–4.3 Sv. However, the LJZF96 value reflects a 3-Sv southward bias applied to the WATTS data in an attempt to account for reduced resolution of the DWBC core relative to the more densely instrumented, earlier STACS-8 experiment. Thus, the actual measured difference between the present transport estimate and that of LJZF96 is 1.2–1.3 Sv, and is presumably due to use of a different computational methodology. This amounts to a difference in the VAV of 0.3 cm s^{-1} in a 4000-m deep ocean over a 100-km section, which is substantially less than the accuracy of the VAV measurement itself. In the sequel, the LJZF96 3-Sv correction will not be used, both because its uncertainty is not easily quantifiable and since the recirculation to the east of the boundary current moorings is at least as poorly resolved as the DWBC core, and hence another, unknown correction would have to be applied to the northward flow as the transport integration continues to the east. This difference in philosophy reflects that the present purpose is analysis of the major characteristics of transport out to large distances (up to 425 km) from Abaco, in contrast to the LJZF96 goal of estimating transport in the southward-flowing DWBC core near the coast.

Figure 13 shows meridional transport time series computed from all of the mooring and HEF data to distances of 85, 125, 225, 325, and 425 km offshore. Note that the HEF data begin at about day 100, and hence the three easternmost traces originate at that time. One of the most robust features of Fig. 13 is the low-frequency variability. The southward transport is strongest in late fall (extending into early winter during the first year) and weakest in the late spring and early summer. However, southward transport is again small at the end of the record in January 1992, an occurrence associated with weak meridional velocities at all sites from A to E around day 550 (Fig. 3) transitioning to an eddylike motion around day 600 (Figs. 2 and 3). LJZF96 consider the end of the record a period when the DWBC

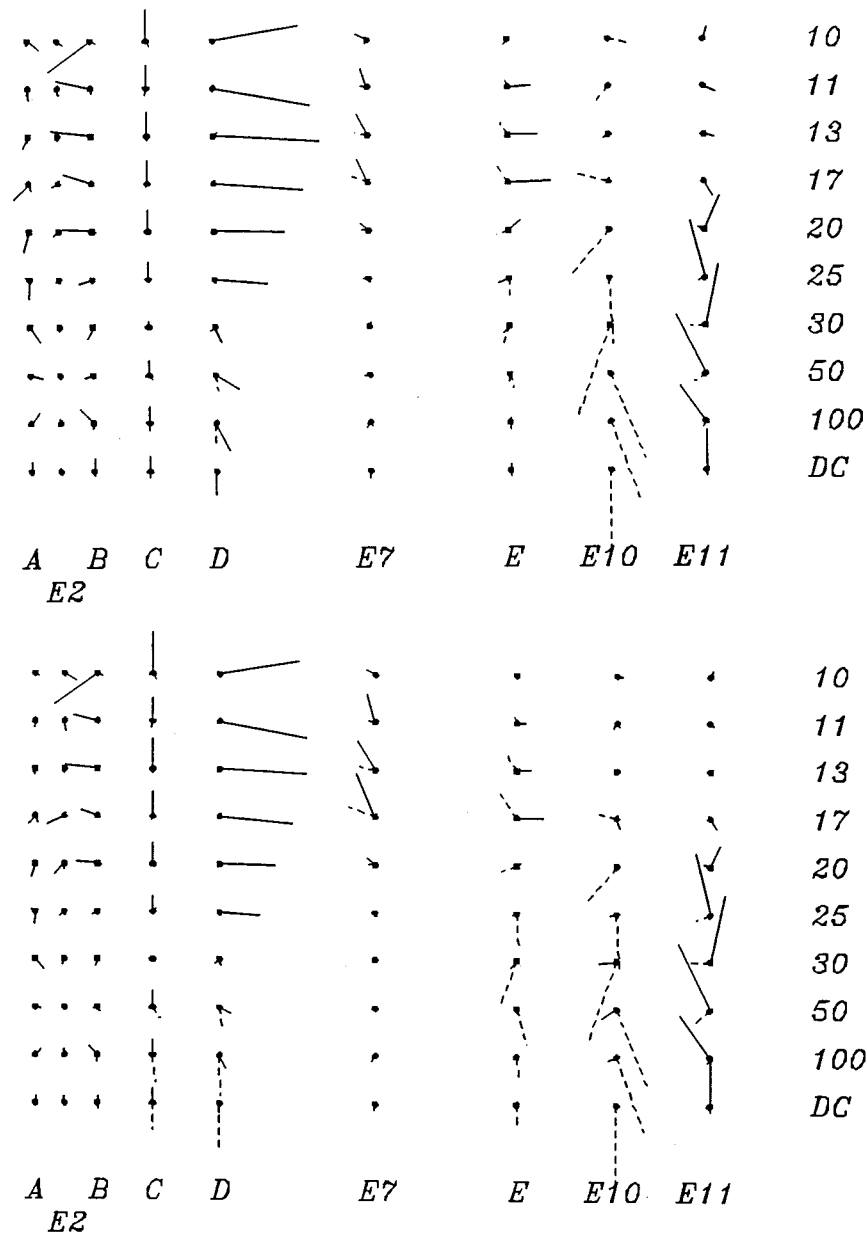


FIG. 10. The first principal component (top) and squared coherence of the first principal component with the data (bottom) for the zonal and meridional vertically averaged velocities at all Abaco line sites. The numbers at the right indicate the center of the period band for which the quantities are plotted. The vertical spacing between lines in the coherence plot is equivalent to a squared coherence of 0.5, and the horizontal spacing of the entries is proportional to the distance between the Abaco line sites. Each of the solid and dashed lines represents either the principal component or squared coherence of the meridional or zonal velocity, respectively, and the orientation gives the phase, with 0° being up and phase increasing in a clockwise manner. The phase reference (0° phase) is the meridional velocity at site C for all periods. The spectra were computed with a time-bandwidth of 10 and 20 Slepian sequences, yielding an approximate bandwidth of 0.03 cpd and about 20 degrees of freedom for the coherence estimate. This yields a zero coherence level at 95% significance of 0.28.

is offshore of mooring D. It is certainly possible that there is unobserved southward flow between D and E7.

LJZF96 attribute much of the variability in the meridional transport computed using only the mooring data

to offshore meandering of the DWBC beyond mooring D. In particular, they identified three intervals in Fig. 13 as being affected by offshore meandering: from days 275–300, 380–490, and 560 to the end of the record.

TABLE 2. Meridional transport statistics in Sverdrups.

Width (km)	Sample mean	Sample standard deviation	Spectral mean	Spectral standard error	Minimum	Maximum
85	-9.7	27.8	-10.9	13.7	-57.8	55.3
125	-18.1	32.9	-19.2	16.5	-80.0	70.6
225	-21.8	23.8	-20.6	10.2	-82.6	34.7
325	-17.0	24.9	-17.0	8.3	-103.1	55.8
425	-33.0	29.5	-32.2	10.5	-139.4	68.6

The addition of E7 between moorings D and E makes it possible to re-examine this conclusion. Comparison of Figs. 3–5 with Fig. 13 suggests that the first of these periods is not affected by meandering; the VAV at sites D, E7, and E is not southward. Rather, this appears to be a real reduction in the core velocity of the DWBC as discussed earlier. By contrast, the second interval is clearly influenced by meandering or the passage of an eddy from an upstream meander; the velocity is southward as far offshore as E7 and northward at sites B and C around day 400 (and the zonal currents are strongly westward). This results in the large northward excursion in meridional transport at 125 km in Fig. 13, which is removed when the VAV is integrated to 225 km offshore. It is nevertheless possible that the meander/eddy is accompanied by a reduction in DWBC transport. The last period again is influenced by meandering and/or a more complex eddying motion than the term meander implies, as the VAV is northward at site B, westward at site C, southward and westward at D, and neutral at E7. The southward flow clearly does not progress as far offshore as E7, unlike for the event between days 380 and 490. Overall, it is clear that some fraction of the variability in Fig. 13 is due to real pulsation in the total transport of the boundary currents.

To compute the mean transport of the DWBC core, LJZF96 discarded about 40% of the WATTS data corresponding to intervals of low southward transport under the hypothesis that a reduction in measured transport is due to eastward meandering of the DWBC out of the boundary current array. This is a reasonable procedure if meandering is the dominant mode of variability, but the present result suggests that pulsation is also present to some degree, and hence culling the data will produce an unknown southward bias in the mean transport. Thus, the 40-Sv DWBC transport derived by LJZF96 should be viewed as an upper limit.

Summary statistics for the 12-h transport time series extending from June 1990 to February 1992 at 85 and 125 km and September 1990 to February 1992 at 225, 325, and 425 km are presented in Table 2. Traditionally, the mean of an oceanographic time series is estimated using the standard sample mean and its standard error is derived from the integral timescale computed using the sample autocorrelation sequence. However, the integral timescale calculation is typically very sensitive

TABLE 3. Comparison of meridional transport estimates in Sverdrups.

Width (km)	LADCP mean	This study
85	-12.1	-9.7
125	-17.0	-18.1
225	-23.4	-21.8
325	-33.0	-17.0
425	-42.7	-33.0

to small trends and periodic components, frequently producing unacceptable results. As an alternative, appendix C presents estimators for the mean and its standard error (hereafter denoted the spectral mean and spectral standard error) based on the multiple window spectrum (D. J. Thomson, personal communication 1995), which has yielded more consistent results. The sample and spectral means in Table 2 are typically within 1 Sv or less of each other, which is smaller than the error with which transport is measured. Since the sample and spectral means are essentially identical, the former will be quoted in the sequel, but standard error estimates will utilize the spectral value. The sample standard deviation and spectral standard error suggest that there are about 4 degrees of freedom near Abaco progressing to more than 8 degrees of freedom to the east.

The addition of E2 to moorings A–D decreases the mean southward transport over the initial 125 km of the Abaco line from -21.7 to -18.1 Sv, a change of 3.6 Sv. The cause is not difficult to discern; E2 displays a meridional VAV that is much weaker than the value on either side of it, and suggests either that the intense core of the northward flowing AC extends farther offshore or that the DWBC is weaker near the Bahamas Escarpment than inferred by LJZF96, at least during WATTS. There is no evidence for large differences in either the T - S (and hence conductivity) or velocity vertical structures at E2 as compared to mooring B, and hence this reduction in the VAV is real (within the accuracy of the HEF measurement) and not due to systematic bias from conductivity weighting of the velocity field. Table 2 also indicates that the recirculation that is apparent at site E7 when the DWBC is close to Abaco does not substantially reduce the mean southward transport, but does

TABLE 4. Meridional transport (less annual term) statistics in Sverdrups.

Width (km)	Annual term	Residual sample mean	Residual sample std. dev.	Residual spectral mean	Residual spectral std. err.	Residual minimum	Residual maximum
85	12.8	-8.0	26.3	-9.1	12.9	-52.5	49.0
125	20.7	-15.3	29.7	-16.0	14.5	-65.1	56.6
225	24.0	-16.6	16.8	-15.4	3.3	-62.1	40.2
325	16.3	-13.6	22.1	-13.6	5.0	-90.3	63.7
425	22.8	-28.1	24.7	-27.4	5.1	-120.7	62.9

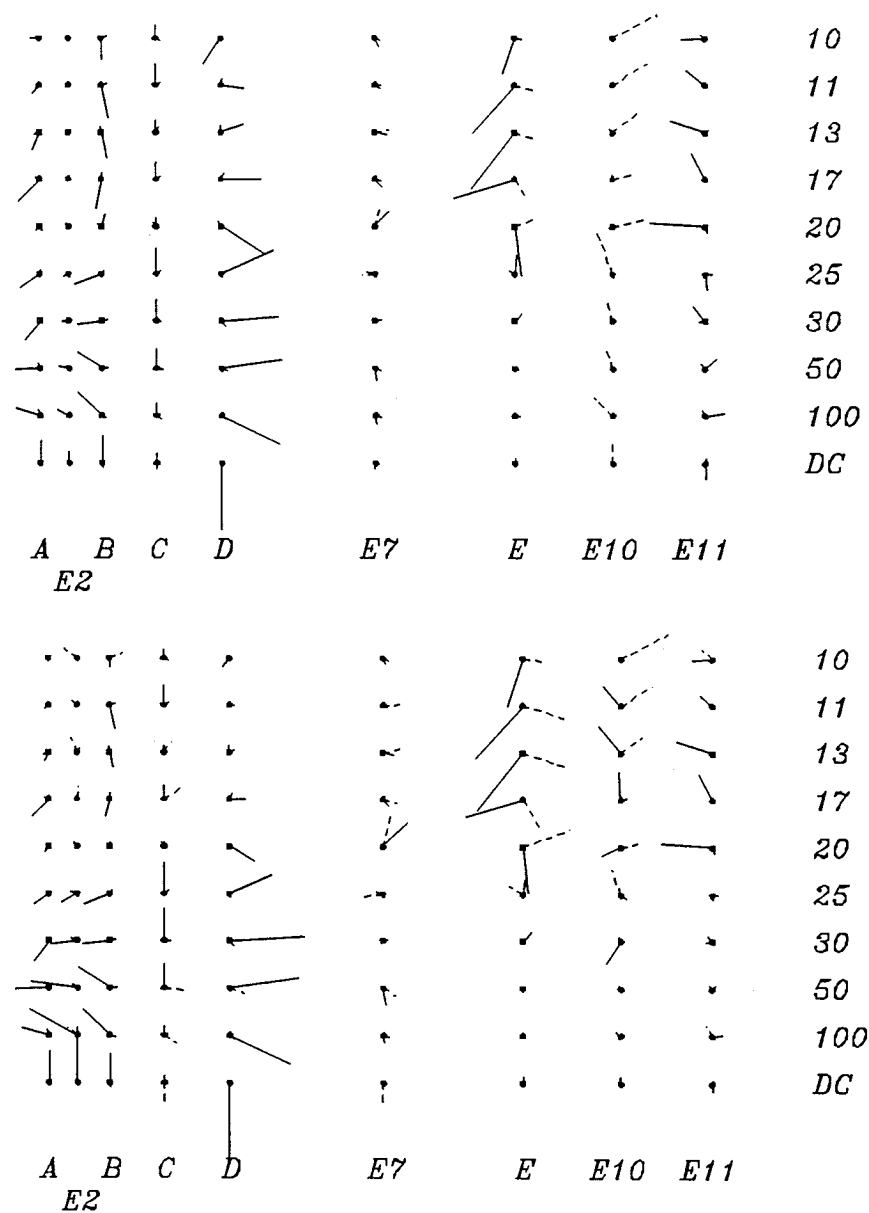


FIG. 11. The second principal component (top) and squared coherence of the second principal component with the data (bottom) for the zonal and meridional vertically averaged velocities at all Abaco line sites. For details see Fig. 10 caption.

reduce the range and standard deviation. In fact, at 225 km, the mean transport is more strongly southward than at 125 km, primarily because the northward transport excursion at 125 km between days 375 and 450 has been removed by extending the zonal integration to the east. The mean transport is reduced as the zonal integration extends to 325 km or to the approximate end of the recirculation zone. The mean southward transport becomes larger as the zonal integration is expanded farther to the east due to the generally southward VAV at E10 and E11.

Table 3 compares the values in Table 2 with the mean

transports integrated to 85–425 km offshore using four of five LADCP sections along 26.5°N reported by Hacker et al. (1996). These data possess comparable to better spatial resolution than the present data out to 400 km offshore. The only exception to this is their June 1993 dataset, which is much sparser in the boundary current region, and hence was not used to avoid sampling bias. The integration methodology applied to the LADCP data is identical to that used for the mooring/HEF data. Despite the different time interval, the mean transports in the boundary current region and out to 225 km are quite similar, especially given the standard errors cited

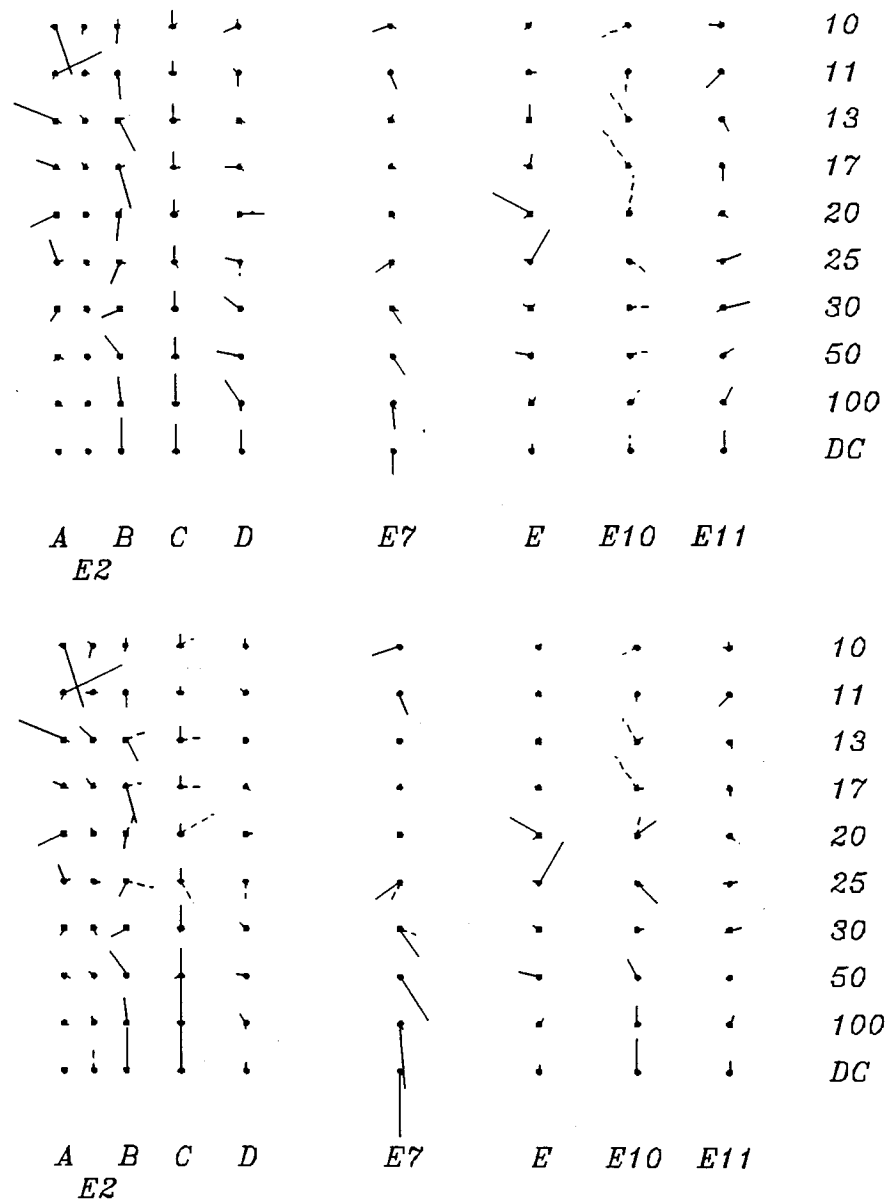


FIG. 12. The third principal component (top) and squared coherence of the third principal component with the data (bottom) for the zonal and meridional vertically averaged velocities at all of the Abaco line sites. For details see Fig. 10 caption.

in Table 2. The 225-km value is not changed if the June 1993 data are included, although the two inshore values are reduced by more than 50%, reflecting a combination of a significant offshore shift of the DWBC core at that time and poor spatial sampling. The LADCP mean transports extending farther to the east are larger than those in Table 2, further supporting the existence of strong southward flow east of the recirculation region. The 325-km LADCP value is slightly more than two standard errors larger than the mooring estimate, but the 425-km value is within one standard error. The 325-km discrepancy may reflect interannual differences, but

could also be due to velocity underestimation from poor vertical sampling at mooring E caused by current meter failures.

Strong low-frequency variability is apparent in Fig. 13, and will certainly bias the mean transports listed in Table 2. LJZF96 used 5.8 years of mooring data to show that there are robust annual and semiannual cycles in the Abaco line transport. They further suggested that the annual cycle is a barotropic response to remote wind forcing that is consistent in amplitude and phase with the numerical model of Böning et al. (1991), whereas the semiannual component is a baroclinic response to

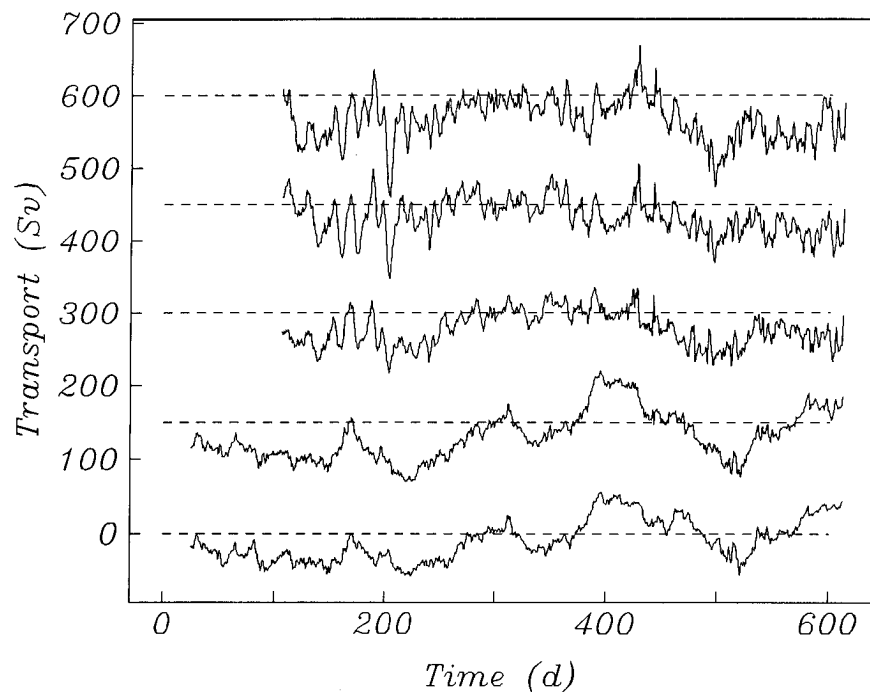


FIG. 13. Time series of the meridional transport computed from the vertically averaged velocity data as described in the text after zonal integration to an offshore distance of 85, 125, 225, 325, and 425 km from bottom to top. Each time series has been offset by 150 Sv, and the dashed line shows zero transport for each. The time reference is 0000 UTC 1 June 1990.

the local wind that is primarily confined to the upper ocean. As a test of the possible bias produced by annual and semiannual components, deterministic components with periods of one-half and one year and a mean were fit to the transport time series by least squares. While the annual term is significant, the addition of the semiannual term does not improve the fit, which is consistent with the idea that this component is baroclinic and hence largely averaged out by vertical integration of the water velocity. Table 4 shows the statistics for the meridional transport after removing the annual term. The residual mean is typically reduced by 10%–15%. Note that the annual term has an amplitude of about 20 Sv, which is substantially larger than the 13 Sv reported by LJZF96 using the 5.8-yr time series and seen in the model results of Böning et al. (1991). Attempts to fit an annual cycle constrained to have an amplitude of only 13 Sv consistently produced a significantly higher residual variance, and this lower value cannot be supported by the available data. The large annual cycle in the WATTS data is due either to interannual variability of the annual cycle or the propitious occurrence of the meander/eddy around day 400.

Figure 14 shows variance conserving power spectra for the meridional transport at 125 and 225 km after removing the annual term. At 125 km, the variance is concentrated at the longest periods, with a very weak peak at about 30 d. At 225 km, the variance is weaker at long periods and spread more widely over frequency.

In particular, the variance is markedly lower at periods over 125 d, presumably because the meandering and recirculation which produce some of the long period variability are not reflected in the transport at 225 km, but dominate the 125-km estimate. There is also a strong peak at 15–20 d; this band dwarfs the long period one when the transport is extended to 325 km. This suggests that the 15–20 d variability has an origin outside of the DWBC near Abaco.

6. Relationship of the Abaco and Florida Straits meridional transports

The Florida Current carries warm water through the Florida Straits northward into the Gulf Stream. The DWBC flowing south past Abaco is the cold thermohaline counterpart to this flow, and local interactions between these two current systems are poorly understood. Thus, it is worth searching for any statistical relations between the meridional transport past Abaco and through the Florida Straits. Fortunately, a continuous time series of FC transport exists through a long-term measurement program using an in-service submarine telephone cable that spans the Florida Straits from West Palm Beach to Eight Mile Rock, Grand Bahama Island. A series of intercomparison studies have shown that the cable yields transport with an accuracy of 1–2 Sv or better (Larsen 1991, 1992). Daily mean values from this cable were obtained that span the WATTS interval (J.C.

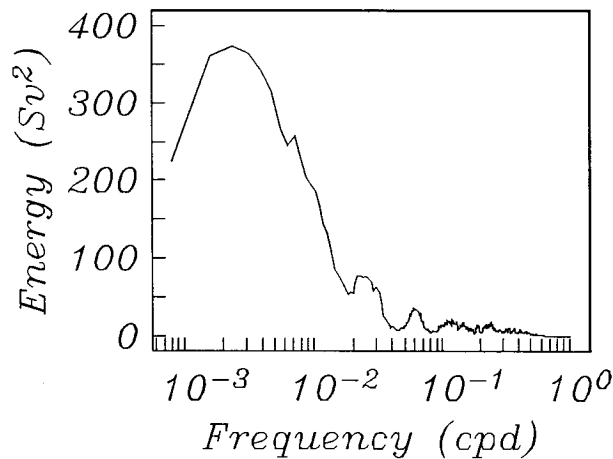
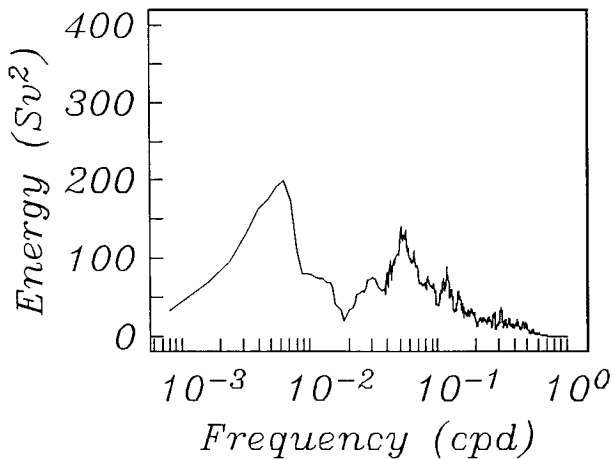


FIG. 14. Multiple window power spectra in variance conserving form for the meridional transport to 225 km (top) and 125 km (bottom) offshore computed using the data from September 1990 (day 260) to the end of the record, the interval when E7 was operational. The bandwidth of the estimate is 0.01 cpd and each frequency has about 14 degrees of freedom.

Larsen, personal communication 1995). These data exhibit weak annual variability (about 2.2 Sv) that is not resolvable with a short record (Larsen 1992), and hence was not removed. Figure 15 shows a variance-preserving power spectrum of the FC transport. Because this data series exhibits a large mean, which could bias the spectral estimate, the raw spectrum was reshaped at zero frequency using the method described by Thomson (1982). Comparison of Figs. 14 and 15 shows that the FC transport has unresolved power at lower frequencies than for the Abaco line, but still shows a weak concentration of variance around 125 d, as well as a variety of shorter period features.

Figure 16 exhibits the multiple window two-point squared coherence between the FC transport and the Abaco line transport out to 125 km with the annual component removed and both spectra reshaped at zero

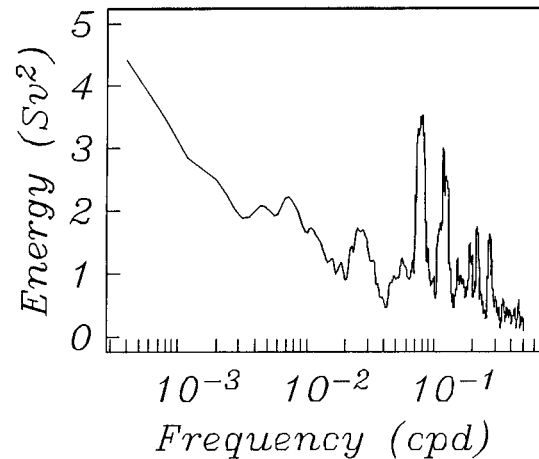


FIG. 15. Multiple window power spectrum in variance conserving form for the Florida Current transport as measured on a submarine cable spanning the Florida Straits from June 1990 to February 1992. The bandwidth of the estimate is 0.01 cpd and each frequency has about 14 degrees of freedom.

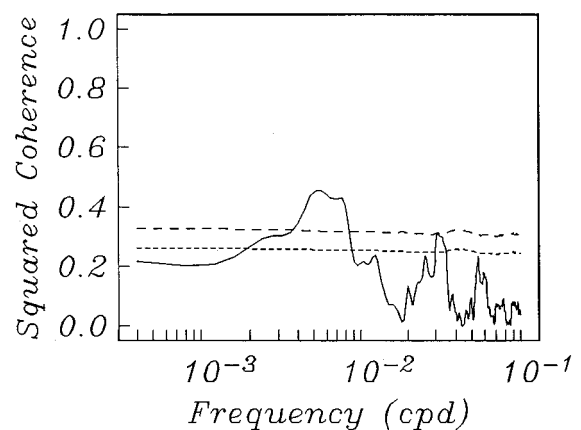
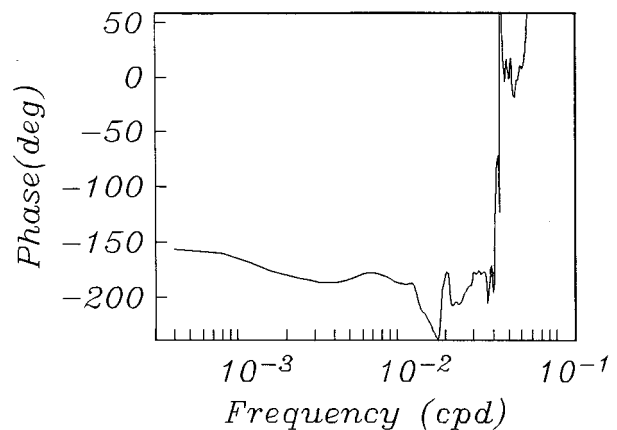


FIG. 16. Squared coherence (bottom) and phase (top) between Florida Current transport and Abaco transport out to 125 km. In the bottom plot, the long and short dashed lines show the zero coherence level at 95% and 90% significance, respectively. A positive phase means that Abaco transport leads Florida Current transport.

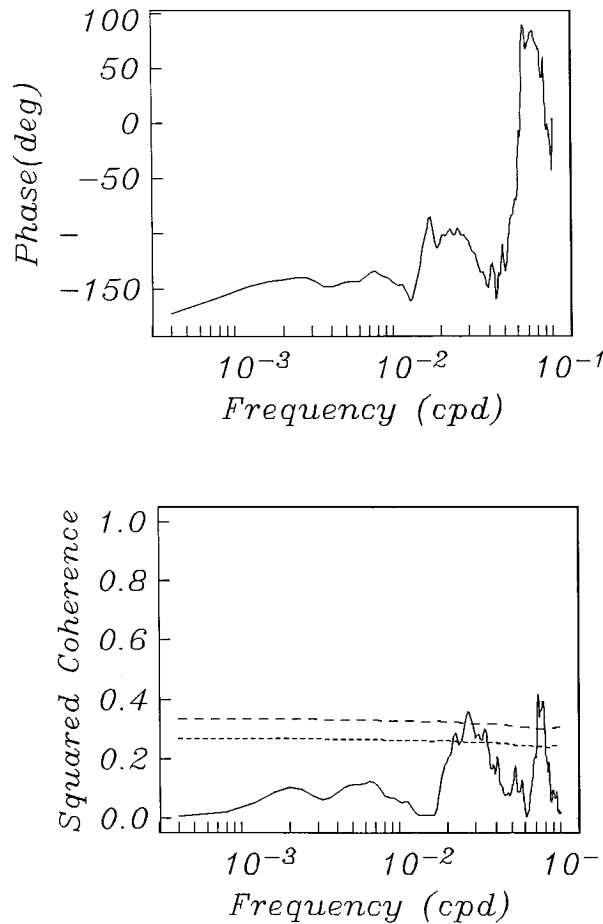


FIG. 17. Squared coherence (bottom) and phase (top) between Florida Current transport and Abaco transport out to 225 km. In the bottom plot, the long and short dashed lines show the zero coherence level at 95% and 90% significance, respectively. A positive phase means that Abaco transport leads Florida Current transport.

frequency. The ensuing squared coherence is significant at the 95% level from 100–250 d, coinciding approximately with variance peaks seen in spectra of both time series. The variability over this band is out of phase, so that an increase in the southward transport at Abaco would correspond to an increase in the northward transport in the FC.

Figure 17 shows the multiple window two-point squared coherence between the FC transport and the Abaco line transport out to 225 km with the annual component removed. Both sets of raw spectra were reshaped to remove the effect of the mean value. The coherence at 100–250 d is not significant, presumably reflecting the weaker signal off Abaco as the recirculating component is removed from the transport time series. There is significant coherence from 20 to 40 and 12 to 15 d. The latter band corresponds to a large variance peak in the FC transport (Fig. 15) and has a phase of about 100°, so that the Abaco line transport is leading the FC transport.

The cause of the observed long-period correlation is difficult to determine without an extensive modeling effort or additional data, both of which are beyond the scope of this paper. Nonlocal forcing from north of 26° that results in shelf or Kelvin waves is unlikely because the disturbance would have to be barotropic to affect transport off Abaco, and the large offshore scale of such a wave would probably yield an in-phase response in the FC and at Abaco. More fundamentally, a simple kinematic explanation for the observed out-of-phase correlation is that relative high pressure (i.e., an east-west relative maximum in pressure) along the east coast of the Bahamas will force flow through the Northwest Providence Channel, thus increasing the FC transport at the cable location. By geostrophy, this will be balanced by a southward flow off the Bahamas, and hence if the high pressure oscillates at long periods, the flows in the FC and off Abaco would be out of phase. However, this does not address the cause of fluctuating pressure at the Bahamas, and there are numerous atmospheric and nonatmospheric candidates.

7. Discussion and conclusions

The additional information provided by the HEF data, especially E2 and E7, alters the picture of the Abaco velocity section given by LJZF96 in four ways. First, the more northward VAV observed at E2 suggests either that the southward flowing DWBC is much weaker near the Bahamas Escarpment, or that the intense core of the northward flowing AC extends farther to the east, or some combination of the two, to explain the 3.6 Sv reduction in net southward transport that ensues when E2 is added to the mooring data for computing meridional transport. It is not possible to uniquely discriminate these mechanisms with the available data.

Second, it appears that E7 catches the recirculation of the DWBC at some times, and may catch the eastern edge of the DWBC during strong meander/eddy events at other times. Examples of the former occur from days 100 to 250 and 450 to 500 (Figs. 2–3). The only example of the latter transpires from days 360 to 410 when the velocity is weakly southward at E7 and D, with a suggestion of intensification as the southward flow appears to move to the west toward site B. However, as noted earlier, there is no evidence for the DWBC meandering offshore to the location of E7 prior to day 360. There is also no indication of northward recirculation at mooring E during the southward event at E7. This is suggestive of more complex behavior than a boundary current system (i.e., a southward DWBC and its northward recirculation), which meanders zonally as a unit.

Third, it is clear that there is some interrelationship between the flow near the boundary and that to offshore distances of at least 425 km. This is especially evident in the principal component analysis. The first principal component (Fig. 10) shows a persistent correlation of the zonal VAV at E and E10 and the meridional VAV

at E11 with the boundary flow at periods longer than 20 d. The second principal component (Fig. 11) displays analogous relationships at shorter periods. The long-period out of phase coherence of E7 and the in phase coherence of B and C with the easternmost sites E10 and E11 are other manifestations of some type of long-range interaction. As noted in section 3, one possible explanation is that the DWBC bifurcates as it turns the sharp corner at the Blake–Bahama Outer Ridge near 29°N, 72°W so that the component flowing along the Blake Escarpment and the offshore part are intimately related.

Finally, it is not possible to ascribe all of the variability of the DWBC to zonal meandering of a meridional current, and fluctuation of the core speed is clearly occurring during the WATTS interval. The estimate of total transport during WATTS at 125 km in Table 2 (−18.1 Sv) compares with the LJZF96 value of −25.9 Sv. Most of the difference between these values can be accounted for by the 3-Sv southward bias applied by LJZF96 to attempt to correct for undersampling of the DWBC during WATTS and the 3.6-Sv reduction in southward transport that ensues when E2 is added to the mooring data. LJZF96 then removed about half of the WATTS data corresponding to presumed offshore meandering of the DWBC out of the boundary current array, leading to an increase in their estimated mean transport for the DWBC (after accounting for 5.1 ± 1.8 Sv of northward AC flow) from −31 Sv to −43 Sv, a change of 12 Sv. This is an estimate for the southward DWBC flow without removing the recirculating component. As an alternate viewpoint, Table 2 suggests that the net transport after correction for recirculation is −17.0 Sv out to 325 km (approximately the location of mooring E). If the 5.1 Sv of northward transport for the AC suggested by LJZF96 is removed, this reflects a net DWBC transport corrected for recirculation of −22.1 Sv. This value could be biased northward by intervals where the DWBC has meandered to a point between D and E7 and hence would be poorly resolved. This may occur for a small part of the time between days 360 and 400 and at the end of the record (Fig. 3), but has clearly not happened during the first half of the WATTS interval, so that any bias will be weak. It is as likely biased southward by inadequate sampling of the recirculation region. This value of the net DWBC transport at 325 km is further reduced to −18.7 Sv when the annual term is removed (Table 4). While it is difficult to be quantitative, this last estimate is probably uncertain by about 4 Sv. Thus, within the uncertainties in the measurements, the observed net DWBC transport after correcting for recirculation is consistent with that postulated to enter the North Atlantic at the Grand Banks. Taking the LJZF96 43 Sv estimate for the mean DWBC transport during WATTS as an upper bound for the southward flow, this suggests that as much as 24 Sv recirculates in the Abaco region.

However, these numbers may not reflect the entire

DWBC transport if the hypothesis that the southward flow at E10 and E11 reveals a split of the current at the Blake–Bahama Outer Ridge is correct. Note that the 425-km mean flow after removal of the annual term is substantially larger than that at 225 or 325 km (Table 4). There is no evidence for an eastern boundary to the southern flow seen at E10 and E11, so this number may be biased low. Furthermore, there must be significant recirculation farther to the east, which was not measured by the HEF recorders but would be required to reduce the net southward transport to that known to round the tail of the Grand Banks. The observations at E10 and E11 may be the western edge of an elongate recirculation gyre extending from the Guiana Basin near the equator to 30°N portrayed by Schmitz and McCartney (1993) and Reid (1994). Answering these questions by direct means would require instrumentation extending at least 600 km off Abaco and cannot be handled with a small number of observation sites close to the boundary. Furthermore, the strong variability exhibited at all points along the Abaco line suggests that a long-term mooring/HEF recorder effort would provide a better understanding of the flow than can be obtained from a few synoptic pictures.

Acknowledgments. This work was supported by NSF Grant OCE89-11977 and by the Office of Global Programs, NOAA under Grant NA16RC0545. The current meter data were collected by Bill Johns and Tom Lee of the University of Miami. Peter Hacker and Eric Firing provided the LADCP data used in section 4. The Florida Current transport data used in section 6 and several helpful discussions were generously provided by J. C. Larsen of NOAA. David Thomson of AT&T Bell Laboratories suggested the multiple window estimator to get the standard error on the mean of a time series derived in appendix C.

APPENDIX A

The HEF–Velocity Relationship

For the low-frequency limit where the aspect ratio of the currents and the effect of self-induction are small and where the vertical velocity may be neglected by comparison to the horizontal components, it can be shown that the HEF at a point is given by (Chave and Luther 1990)

$$\vec{E}_h = CF_z \hat{z} \times \langle \vec{v}_h \rangle^* + \frac{\vec{J}^*}{\sigma} + \vec{N}, \quad (\text{A1})$$

where angle brackets denote the average of the enclosed function from seafloor to sea surface and

$$\langle \vec{v}_h \rangle^* = \frac{\langle \sigma \vec{v}_h \rangle}{\langle \sigma \rangle} \quad (\text{A2})$$

is the seawater conductivity-weighted, vertically integrated water velocity, \vec{v}_h is the horizontal water velocity,

σ is seawater electrical conductivity, and F_z is the vertical component of the geomagnetic field. The scale factor $C \leq 1$ accounts for reductions in the observed electric field due to current leakage and dissipation in the conducting earth beneath the seafloor. Geophysical evidence suggests that $C \approx 0.95$ with about 5% uncertainty in the deep ocean (Chave and Luther 1990), with most of the variability being due to changes in sediment thickness. Based on contemporaneous towed electric field measurements along 26.5°N and intercomparison with mooring data, Sanford et al. (1994) estimate $C = 0.95$ for the study area, and this value has been adopted for the analyses in this paper. The geomagnetic field, including its secular variation, may be obtained from standard spherical harmonic expansions. The remaining terms in (A1) represent possible errors due, respectively, to local and nonlocal electric currents and to externally (i.e., magnetospherically) produced geomagnetic noise. The latter is negligible at periods longer than a few days at midlatitudes (Chave et al. 1989) and will be ignored. Based on observations, the first term in (A1) dominates the effect of electric currents even near coastlines (Sanford 1986; Luther and Chave 1993). Furthermore, the second term in (A1) has been shown to be small compared to the first term in (A1) throughout the North Atlantic using high-resolution numerical models (Flosadottir et al. 1997a, 1997b), and hence \vec{J}^* will be ignored.

When the last two terms in (A1) are neglected, the equation may be inverted to give

$$\langle \vec{v}_h \rangle^* = -\hat{z} \times \frac{\vec{E}_h}{CF_z}, \quad (\text{A3})$$

which is the fundamental oceanographic quantity determined from low-frequency electric field measurements in the ocean. Writing the seawater conductivity σ as the sum of a vertical average part $\langle \sigma \rangle$ plus a depth-dependent residual $\tilde{\sigma}$, (A3) may be reexpressed as

$$\langle \vec{v}_h \rangle^* = \langle \vec{v}_h \rangle + \frac{\langle \tilde{\sigma} \vec{v}_h \rangle}{\langle \sigma \rangle}, \quad (\text{A4})$$

where the first term is just the VAV and the second term is generally small because seawater conductivity is a weak function of depth. To a good approximation, $\sigma = 3.0 + 0.09T$ in siemens per meter, where T is temperature in degrees Celsius, and hence $\langle \sigma \rangle \approx 3.4 \text{ S m}^{-1}$ with $\tilde{\sigma}$ being the small remainder. Note also that the second term in (A4) is small if the water velocity has little vertical shear.

It is possible to use the mooring data to estimate the relative size of the two terms on the right-hand side of (A4) and hence bound the accuracy with which the HEF measures the VAV. For this purpose, it is convenient to expand the velocity and temperature time series at each mooring in terms of dynamical normal modes. The first term in (A4) is the VAV, whose estimation is described in section 2b. Time series of seawater conductivity at

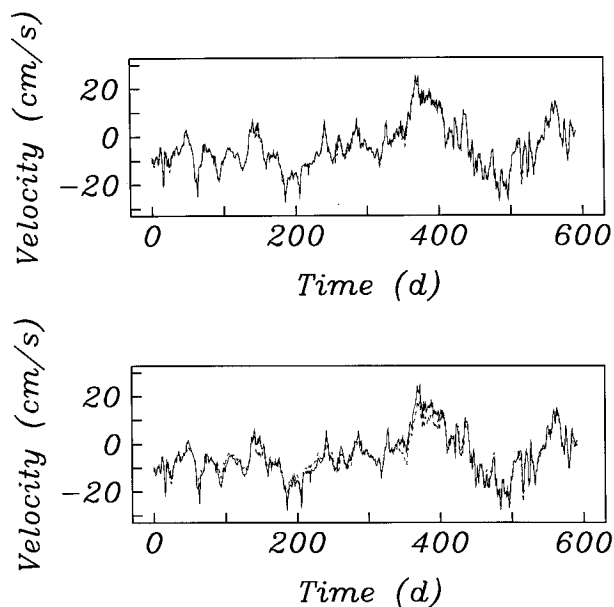


FIG. A1. (top) Comparison of the vertically averaged meridional velocity $\langle \vec{v}_h \rangle$ (dashed line) with the vertically averaged, seawater conductivity weighted meridional velocity $\langle \vec{v}_h \rangle^*$ (solid line) at site C using all of the available data at 180, 480, 880, 1280, 2080, 3080, and 4080 m. The time reference is 0000 UTC 1 June 1990. The rms difference between the two curves is 0.92 cm s^{-1} . (bottom) Comparison of the vertically averaged meridional velocity $\langle \vec{v}_h \rangle$ (solid line) with the averaged velocity below 800 m (dashed line) at site C. The mean (rms) difference between the two traces is 0.34 (2.3) cm s^{-1} .

each instrument can be constructed where temperature records exist by using a regional T - S relationship obtained by averaging 174 CTD casts extending from Abaco to 70°W over 1984–1992 (E. Johns, personal communication 1994) to compute salinity from temperature, then inverting in situ temperature, salinity, and pressure for conductivity using standard algorithms (Fofonoff and Millard 1983). The salinity effect on conductivity is weak, with 0.1 psu variation at 5°C contributing about a 0.25% change, and hence the result does not depend strongly on the assumed T - S relationship. Dynamical normal modes may then be fit to the conductivity time series by least squares, and the second term in (A4) follows in a manner like that for the first.

Figure A1 (top) compares $\langle \vec{v}_h \rangle^*$ and $\langle \vec{v}_h \rangle$ computed for the meridional velocity component at mooring C. The two are nearly indistinguishable, with the largest discrepancy occurring at peaks in the velocity, which also correspond to intervals of significant mooring motion. This example is typical; the rms difference averaged over moorings B–E is 1.1 cm s^{-1} . Table 5 provides summary mean and standard deviation statistics for the lhs and both rhs terms in (A4) for moorings B–E; mooring A is omitted because there are only two current meter records over most of the interval. Agreement in the mean between $\langle \vec{v}_h \rangle^*$ and $\langle \vec{v}_h \rangle$ is typically better than 1 cm s^{-1} , with only the meridional component at mooring B exceeding this amount. There is also good con-

TABLE A1. Synthetic HEF comparison (in cm s^{-1}).

Site/ component	$\overline{\langle \mathbf{v}_h \rangle^*}$	$\sigma_{\langle \mathbf{v}_h \rangle^*}$	$\overline{\langle \mathbf{v}_h \rangle}$	$\sigma_{\langle \mathbf{v}_h \rangle}$	$\overline{\langle \sigma \mathbf{v}_h \rangle} / \langle \sigma \rangle$	$\sigma_{\langle \sigma \mathbf{v}_h \rangle} / \langle \sigma \rangle$
B zonal	-4.3	5.9	-3.6	5.8	-0.7	0.8
B meridional	-5.0	14.5	-6.3	14.5	1.3	0.8
C zonal	-5.7	9.2	-5.0	9.3	-0.7	1.0
C meridional	-4.3	9.4	-4.9	9.3	0.5	0.8
D zonal	-7.0	10.5	-6.4	10.8	-0.6	1.1
D meridional	-3.8	8.6	-3.9	8.6	0.1	1.0
E zonal	1.1	5.4	1.0	5.1	0.0	0.8
E meridional	-0.2	3.7	-0.2	3.3	0.0	0.8

sistency of their standard deviations. The last term in (A4) is typically much smaller than 1 cm s^{-1} . These results suggest that the HEF (which yields $\overline{\langle \mathbf{v}_h \rangle^*}$) can measure the VAV with a total error of about 1 cm s^{-1} in the Abaco region without making any corrections for seawater conductivity weighting of the water velocity. This serves as an upper bound on the bias error associated with conductivity weighting since the values quoted in Table 4 also include the effects of statistical variability, and is comparable to the accuracy with which the VAV can be measured at a single current meter mooring.

Figure A1 (bottom) compares the VAV for the meridional velocity at mooring C with the averaged velocity for depths greater than 800 m, which should be dominated by the DWBC. The mean (rms) difference of the two curves is 0.34 (2.3) cm s^{-1} . The figure shows that the largest differences occur at peaks in the velocity when the arbitrary 800-m cutoff may not completely sample the DWBC and when error due to mooring motion is especially significant. These intervals are emphasized in the rms difference statistic. This example is typical of the meridional velocity at moorings B–D; the mean (rms) difference between the VAV and the averaged velocity below 800 m for the three moorings is 0.58 (2.5) cm s^{-1} . These results suggest that the VAV is dominated by DWBC variability near Abaco.

APPENDIX B

Multiple Window Principal Components Analysis

Consider a set of p time series $x_j(n)$, $n = 0, \dots, N - 1$, $j = 1, \dots, p$. It is assumed that the univariate adaptive spectral weights d_k^j for each series described by Thomson (1982) with the modifications given in the appendix to Vernon et al. (1991) are available and that deterministic portions of the spectrum have been removed by reshaping. It is also assumed that the time-bandwidth product NW for the spectral estimate has been chosen so that the number of orthogonal data tapers $K < p \leq 2NW$. Define the $K \times p$ spectral matrix \mathbf{S} whose k, j element at a given frequency is given by

$$s_k^j = a_k^j w_k^j, \quad (\text{B1})$$

where

$$a_k^j = \left(\frac{A \lambda_k}{K \sum_{k=0}^{K-1} (d_k^j)^2} \right)^{1/2} \quad (\text{B2})$$

and

$$w_k^j = \sum_{n=0}^{N-1} e^{-i2\pi f n} \nu_n^{(k)}(N, W) x_j(n) \quad (\text{B3})$$

is the discrete Fourier transform of the j th time series at frequency $0 \leq f \leq 0.5$ computed using the k th Slepian or discrete prolate spheroidal sequence $\nu_n^{(k)}$ as a data window. The properties of Slepian sequences are thoroughly described by Percival and Walden (1993). The remaining quantities in (B2) and (B3) are the eigenvalue λ_k corresponding to the k th Slepian sequence, which gives the fractional energy concentration in the band $-W \leq f \leq W$,

$$A = \sum_{k=0}^{K-1} \lambda_k^{-1} \quad (\text{B4})$$

and the univariate adaptive weight d_k^j for the j th time series and k th taper at frequency f . Define a general preweighting of the columns of \mathbf{S} by postmultiplying it by the diagonal matrix \mathbf{B} . The elements of \mathbf{B} will contain the reciprocal of the square roots of the autopowers for the different channels if \mathbf{S} is to have unit variance, and is otherwise the identity matrix. Apply the singular value decomposition to get

$$\mathbf{SB} = \mathbf{U}\mathbf{\Sigma}\mathbf{V}^H, \quad (\text{B5})$$

where the columns of \mathbf{U} and \mathbf{V} , which are orthogonal and unitary, contain the left and right singular vectors, respectively, $\mathbf{\Sigma}$ contains the singular values in its first p diagonal locations, and the superscript H denotes the Hermitian transpose. The right singular vectors in \mathbf{V} are the orthogonal factors that most succinctly describe the variability in the dataset and are identical to the eigenvectors of the matrix of auto- and cross-powers, which are sometimes called empirical orthogonal functions. The squared singular values represent the power associated with each eigenvector.

Define the $K \times p$ matrix of principal components or empirical orthogonal function amplitudes \mathbf{Z} by

$$\mathbf{SB} = \mathbf{Z}\mathbf{V}^H. \quad (\text{B6})$$

These serve to project the data in \mathbf{S} onto the right singular vectors. From (B5), it can be shown that $\mathbf{Z}^H\mathbf{Z} = \mathbf{\Sigma}^2$, and hence the principal components are the dimensional orthogonal modes of variation of the data.

Define the cross-spectrum between the j th principal component and the i th data channel

$$\mathbf{Q} = \mathbf{Z}^H\mathbf{S} = \mathbf{\Sigma}^2\mathbf{V}^H\mathbf{B}^{-1}, \quad (\text{B7})$$

whose i, j element is

$$q_i^j = \sigma_j^2 v_i^{j*} / b_i. \quad (\text{B8})$$

The coherence between the j th principal component and

the i th data channel may be computed from (B8) and its significance may be assessed in the usual way. Only those principal components whose coherence with the data exceeds a threshold value should be given a physical interpretation.

APPENDIX C

Estimation of the Standard Error of the Mean

Percival and Walden (1993, p. 188) show that the asymptotic variance for a large sample estimate of the mean of a time series is given by

$$\text{var}\{\bar{x}\} = \frac{S(0)}{N}, \tag{C1}$$

where $S(0)$ is the true power spectral density at zero frequency assuming a unit sample interval and N is the length of the time series. Equation (C1) is formally equivalent in the large sample limit to using the autocorrelation sequence to determine the integral timescale from which the equivalent degrees of freedom can be estimated and applied to the sample variance.

The sample mean \bar{x} is normally computed using the usual estimator: the sum of the elements divided by N . An alternative frequency domain estimator can be obtained using the multiple window method of Thomson (1982). Let $\nu_n^{(k)}$ denote the k th Slepian or discrete prolate spheroidal sequence. The Fourier transform of a data series $x(n)$ with the k th Slepian sequence is given by

$$y_k(f) = \sum_{n=0}^{N-1} e^{-i2\pi fn} \nu_n^{(k)}(N, W)x(n), \tag{C2}$$

where W is half of the bandwidth of the estimate. Thomson (1982) has shown that a least squares estimator for the amplitude of a possible line component at frequency f (which includes zero frequency) is given by

$$\hat{\mu}(f) = \frac{\sum_{k=0}^{K-1} U_k^*(0)y_k(f)}{\sum_{k=0}^{K-1} |U_k(0)|^2}, \tag{C3}$$

where $U_k(0)$ is the k th Slepian function at zero frequency obtained from the discrete Fourier transform of $\nu_n^{(k)}$ and $K \leq 2NW$ is the number of Slepian sequences that are employed. An alternative estimator for the sample mean is (C3) at $f = 0$, and will be called the spectral mean. The standard error may be computed using the residual spectrum $\hat{S}(0)$

$$\hat{S}(0) = \frac{\sum_{k=0}^{K-1} |y_k(0) - \hat{\mu}(0)U_k(0)|^2}{\lceil K/2 \rceil - 1}, \tag{C4}$$

where $\lceil M \rceil$ denotes the greatest integer in the enclosed quantity and the denominator in (C4) follows because the $\{U_k(0)\}$ are zero for odd k . The spectral standard

error is given by the square root of (C1) with (C4) substituted for $S(0)$. This estimator for the standard error typically displays insensitivity to the nature of the data, unlike those based on estimates of the autocorrelation sequence. However, when the residual spectrum is red, there is a small decrease in the standard error as the bandwidth of (C4) rises. Concomitantly, the presence of low-frequency deterministic components within W of zero frequency will cause the spectral standard error to increase.

REFERENCES

Böning, C. W., R. Doscher, and R. Budich, 1991: Seasonal transport variation in the western subtropical North Atlantic: Experiments with an eddy-resolving model. *J. Phys. Oceanogr.*, **21**, 1271–1289.

Bryan, F., and W. Holland, 1989: A high resolution simulation of the wind- and thermohaline-driven circulation in the North Atlantic Ocean. *Proc. 'Aha Huliko' a Hawaiian Winter Workshop on Parameterization of Small Scale Processes*, P. Muller and D. Henderson, Eds., University of Hawaii, 99–115.

Chave, A. D., and D. S. Luther, 1990: Low-frequency, motionally induced electromagnetic fields in the ocean. 1: Theory. *J. Geophys. Res.*, **95**, 7185–7200.

—, J. H. Filloux, D. S. Luther, L. K. Law, and A. White, 1989: Observations of motional electromagnetic fields during EM-SLAB. *J. Geophys. Res.*, **94**, 14 153–14 166.

Filloux, J. H., 1987: Instrumentation and experimental methods for oceanic studies. *Geomagnetism and Geoelectricity*, Vol. 1, J. Jacobs, Ed., Academic Press, Chapter 3, pp. 143–247.

Fine, R. A., 1995: Tracers, time scales, and the thermohaline circulation: The lower limb in the North Atlantic Ocean. *Rev. Geophys.*, **33** (Suppl.), 1353–1365.

Flosadottir, A. H., J. C. Larsen, and J. T. Smith, 1997a: Motional induction in North Atlantic circulation models. *J. Geophys. Res.*, in press.

—, —, and —, 1997b: The relation of seafloor voltages to ocean transports in North Atlantic circulation models: Model results and practical considerations for transport monitoring. *J. Phys. Oceanogr.*, **27**, 1547–1565.

Fofonoff, N. P., and R. G. Millard Jr., 1983: Algorithms for computation of fundamental properties of seawater. *UNESCO Tech. Pap. in Marine Sci.*, 44, UNESCO, Paris, France, 53 pp.

Hacker, P., E. Firing, W. D. Wilson, and R. L. Molinari, 1996: Direct observations of the current structure east of the Bahamas. *Geophys. Res. Lett.*, **23**, 1127–1130.

Hogg, N. G., and W. E. Johns, 1995: Western boundary currents. *Rev. Geophys.*, **33** (Suppl.), 1311–1334.

Jones, R. E., 1969: Approximate integrator of functions tabulated at arbitrarily spaced abscissas. Sandia National Laboratories Rep. SC-M-69-335, 10 pp. [Available from Sandia National Laboratories, Albuquerque, NM 87185.]

Johns, E., R. A. Fine, and R. L. Molinari, 1997: Recirculation of the deep western boundary current south of the Blake Bahama Outer Ridge. *J. Phys. Oceanogr.*, in press.

Larsen, J. C., 1991: Transport measurements from in-service undersea telephone cables. *IEEE J. Oceanic Eng.*, **16**, 313–318.

—, 1992: Transport and heat flux of the Florida Current at 27°N derived from cross-section voltages and profiling data: Theory and observations. *Philos. Trans. R. Soc. London A*, **338**, 169–236.

Leaman, K. D., and J. Harris, 1990: On the average absolute transport of the deep western boundary current east of Abaco Island, the Bahamas. *J. Phys. Oceanogr.*, **20**, 467–475.

—, and P. S. Vertes, 1996: Topographic influences on recirculation in the deep western boundary current: Results from RAFOS float

- trajectories between the Blake–Bahama Outer Ridge and the San Salvador “gate.” *J. Phys. Oceanogr.*, **26**, 941–961.
- , R. L. Molinari, and P. S. Vertes, 1987: Structure and variability of the Florida Current at 27°N: April 1982–July 1984. *J. Phys. Oceanogr.*, **17**, 565–583.
- Lee, T. N., W. Johns, F. Schott, and R. Zantopp, 1990: Western boundary current structure and variability east of Abaco, Bahamas, at 26.5°N. *J. Phys. Oceanogr.*, **20**, 446–466.
- , —, R. J. Zantopp, and E. R. Fillenbaum, 1996: Moored observations of western boundary current variability and thermohaline circulation at 26.5°N in the subtropical North Atlantic. *J. Phys. Oceanogr.*, **26**, 962–983.
- Levitus, S., 1982: *Climatological Atlas of the World Ocean*. NOAA Prof. Paper No. 13, U.S. Govt. Printing Office, 172 pp.
- Luther, D. S., and A. D. Chave, 1993: Observing “integrating” variables in the ocean. *Proc. 7th ‘Aha Huliko’ a Hawaiian Winter Workshop on Statistical Methods in Physical Oceanography*, P. Muller and D. Henderson, Eds., University of Hawaii, 103–130.
- Percival, D. B., and A. T. Walden, 1993: *Spectral Analysis for Physical Applications*. Cambridge University Press, 583 pp.
- Reid, J. L., 1994: On the total geostrophic circulation of the North Atlantic Ocean: Flow patterns, tracers, and transports. *Progress in Oceanography*, Vol. 33, Pergamon Press, 1–92.
- Sanford, T. B., 1971: Motionally-induced electric and magnetic fields in the sea. *J. Geophys. Res.*, **76**, 3476–3492.
- , 1986: Recent improvements in ocean current measurement from motional electric fields and currents. *Proc. IEEE Third Working Conf. on Current Measurements*, Airlie, VA, IEEE, 65–76.
- , R. G. Drever, J. H. Dunlap, and W. E. Johns, 1994: Barotropic flows observed by the towed transport meter. *Proc. IEEE Fifth Working Conf. on Current Measurements*, Miami, FL, IEEE, 24–29.
- Schmitz, W. J., Jr., 1995: On the interbasin-scale thermohaline circulation. *Rev. Geophys.*, **33**, 151–173.
- , and P. L. Richardson, 1991: On the sources of the Florida Current. *Deep-Sea Res.*, **38**(Suppl. 1), S379–S409.
- , and M. S. McCartney, 1993: On the North Atlantic circulation. *Rev. Geophys.*, **31**, 29–50.
- , J. D. Thompson, and J. R. Luyten, 1992: The Sverdrup circulation for the Atlantic along 24°N. *J. Geophys. Res.*, **97**, 7251–7256.
- Thomson, D. J., 1982: Spectrum estimation and harmonic analysis. *Proc. IEEE*, **70**, 1055–1096.
- , and A. D. Chave, 1991: Jackknife error estimates for spectra, coherences, and transfer function. *Advances in Spectral Analysis and Array Processing*, Vol. 1, S. Haykin, Ed., Prentice-Hall, 58–113.
- Vernon, F. L., J. Fletcher, L. Carroll, A. Chave, and E. Sembera, 1991: Coherence of seismic body waves from local events as measured by a small-aperture array. *J. Geophys. Res.*, **96**, 11 981–11 996.
- Zantopp, R. J., T. N. Lee, and W. E. Johns, 1994: Moored current meter observations east of Abaco, The Bahamas (“WATTS” Array). (updated 10/94), Rosenstiel School of Marine and Atmospheric Science Tech. Rep. 93-006, 77 pp. [Available from RSMAS, University of Miami, Miami, FL 33149.]